CrossMark

Einstein Probe Discovery of EP J182730.0−095633: A New Black Hole X-Ray Binary Candidate in Faint Outburst?

H. Q. Cheng[1], Q. C. Zhao[2,3], L. Tao[2], H. Feng[2], F. Coti Zelati[4,5], H. W. Pan[1], A. L. Wang[2], Y. N. Wang[1], M. Y. Ge[2], A. Rau[6], A. Marino[4,5], L. Zhang[2], W. J. Zhang[1], F. Carotenuto[7], L. Ji[8], C. C. Jin[1,3,9], D. Y. Li[1], B. F. Liu[1,3], Y. Liu[1], E. L. Qiao[1,3], N. Rea[4,5], R. Soria[10,11], S. Wang[1], Z. Yan[12], W. Yuan[1,3], B. Zhang[13,14], G. B. Zhang[15,16], S. N. Zhang[2,3], W. D. Zhang[1], A. Beardmore[17], J. S. Bright[18], X. L. Chen[19], Z. Fan[1,3], S. Y. Fu[1], J. P. U. Fynbo[20,21], J. W. Hu[1], J. J. Jin[1], P. G. Jonker[22], A. K. H. Kong[23], E. Kuulkers[24], C. K. Li[2], H. L. Li[1], Z. K. Lin[1], C. X. Liu[19], H.-Y. Liu[1], J. Z. Liu[25,3], X. W. Liu[19], Z. Lu[26,27], C. Maitra[6], H. Y. Mu[1], C.-Y. Ng[28], Y. L. Qiu[1], S. Tinyanont[29], Y. Wang[30], S. X. Wen[1], S. S. Weng[31], Jianfeng Wu[32], D. Xu[1], Y. K. Yan[26], Z. Yan[15], Y.-P. Yang[19], P. Zhang[26,27], S. Zhang[2], Q. Zhao[1], Z. M. Cai[33], Y. Chen[2], Y. F. Chen[34], C. Z. Cui[1,3], W. W. Cui[2], H. B. Hu[1], M. H. Huang[1,3], S. M. Jia[2], G. Jin[35], Z. X. Ling[1,3,9], H. Q. Liu[33], S. L. Sun[34], X. J. Sun[34], Y. F. Xu[1,3], C. Zhang[1,3], M. Zhang[1], and Y. H. Zhang[33]

[1] National Astronomical Observatories, Chinese Academy of Sciences, 20A Datun Road, Beijing 100101, People's Republic of China
[2] Key Laboratory of Particle Astrophysics, Institute of High Energy Physics, Chinese Academy of Sciences, Beijing 100049, People's Republic of China; taolian@ihep.ac.cn
[3] School of Astronomy and Space Science, University of Chinese Academy of Sciences, 19A Yuquan Road, Beijing 100049, People's Republic of China
[4] Institute of Space Sciences (ICE), CSIC, Campus UAB, Barcelona, E-08193, Spain
[5] Institut d'Estudis Espacials de Catalunya (IEEC), Barcelona, E-08034, Spain
[6] Max Planck Institute for Extraterrestrial Physics, Garching, 85748, Germany
[7] INAF-Osservatorio Astronomico di Roma, Via Frascati 33, I-00078, Monte Porzio Catone (RM), Italy
[8] School of Physics and Astronomy, Sun Yat-Sen University, Zhuhai 519082, People's Republic of China
[9] Institute for Frontier in Astronomy and Astrophysics, Beijing Normal University, Beijing 102206, People's Republic of China
[10] INAF-Osservatorio Astrofisico di Torino, Pino Torinese, I-10025, Italy
[11] Sydney Institute for Astronomy, School of Physics A28, The University of Sydney, NSW 2006, Australia
[12] Shanghai Astronomical Observatory, Chinese Academy of Sciences, 80 Nandan Road, Shanghai, 200030, People's Republic of China
[13] Nevada Center for Astrophysics, University of Nevada, Las Vegas, Las Vegas, NV 89154, USA
[14] Department of Physics and Astronomy, University of Nevada, Las Vegas, Las Vegas, NV 89154, USA
[15] Yunnan Observatories, Chinese Academy of Sciences, Kunming 650216, People's Republic of China
[16] Key Laboratory for the Structure and Evolution of Celestial Objects, Chinese Academy of Sciences, Kunming 650216, People's Republic of China
[17] School of Physics and Astronomy, University of Leicester, University Road, Leicester, LE1 7RH, UK
[18] Astrophysics, Department of Physics, University of Oxford, Keble Road, Oxford OX1 3RH, UK
[19] South-Western Institute for Astronomy Research, Yunnan University, Kunming, Yunnan 650504, People's Republic of China
[20] Cosmic Dawn Center (DAWN), Denmark
[21] Niels Bohr Institute, University of Copenhagen, Jagtvej 128, 2200, Copenhagen N, Denmark
[22] Department of Astrophysics/IMAPP, Radboud University, P.O. Box 9010, 6500 GL, Nijmegen, The Netherlands
[23] Institute for Cosmic Ray Research, The University of Tokyo, Kashiwa City, Chiba 277-8582, Japan
[24] ESA/ESTEC, Noordwijk, 2201 AZ, The Netherlands
[25] Xinjiang Astronomical Observatory, Chinese Academy of Sciences, Urumqi 830011, People's Republic of China
[26] College of Mathematics and Physics, China Three Gorges University, Yichang 443002, People's Republic of China
[27] Center for Astronomy and Space Sciences, China Three Gorges University, Yichang 443002, People's Republic of China
[28] Department of Physics, University of Hong Kong, Pokfulam Road, Hong Kong, People's Republic of China
[29] National Astronomical Research Institute of Thailand, 260 Moo 4, Donkaew, Maerim, Chiang Mai, 50180, Thailand
[30] Key Laboratory of Dark Matter and Space Astronomy, Purple Mountain Observatory, Chinese Academy of Sciences, Nanjing 210023, People's Republic of China
[31] Department of Physics and Institute of Theoretical Physics, Nanjing Normal University, Nanjing, People's Republic of China
[32] Department of Astronomy, Xiamen University, Xiamen, Fujian 361005, People's Republic of China
[33] Innovation Academy for Microsatellites, Chinese Academy of Sciences, Shanghai 201210, People's Republic of China
[34] Shanghai Institute of Technical Physics, Chinese Academy of Sciences, Shanghai 200083, People's Republic of China
[35] North Night Vision Technology Co., LTD, Nanjing, People's Republic of China

Abstract

Black hole X-ray binaries (candidates) currently identified in our Galaxy are mainly transient sources, with the majority discovered through the detection of their X-ray outbursts. Among these, only four were found during faint outbursts exhibiting peak X-ray luminosities $L_X \lesssim 10^{36}$ erg s^{-1}, likely due to the previous lack of sensitive, wide-field monitoring instruments in the X-ray band. In this Letter, we present the discovery of an intriguing X-ray transient, EP J182730.0−095633, via the Einstein Probe (EP) and subsequent multiwavelength follow-up studies. This transient, located on the Galactic plane, experienced a faint and brief X-ray outburst lasting about 20 days. Its X-ray spectrum is nonthermal and consistent with a power-law model with a nearly constant photon index of $\Gamma \sim 2$ throughout the outburst. A long-lasting mHz quasiperiodic oscillation signal was detected in its

X-ray light curve, centered around a frequency of $\sim$0.04 Hz. A transient near-infrared source was identified as its counterpart, although no optical emission was detectable, likely due to significant extinction. A radio counterpart was also observed, displaying an inverted radio spectrum with $\alpha \sim 0.45$. The X-ray spectral and temporal characteristics, along with the multiwavelength properties, indicate that the source is a faint low-mass X-ray binary, with the compact object likely being a black hole. This work demonstrates the potential of the EP in discovering new X-ray binaries by capturing faint-level X-ray outbursts.

Unified Astronomy Thesaurus concepts: Low-mass x-ray binary stars (939); X-ray transient sources (1852); Black holes (162)

1. Introduction

Black holes (BHs) are among the most mysterious celestial objects in the Universe. They provide a unique laboratory for studying the general relativity effects and other physical processes in strong gravitational fields. As the inevitable evolutionary destiny and remnant of massive stars, stellar-mass BHs, with masses in the typical range of several to several tens of solar masses, are of great importance in understanding the formation and growth of BHs, as well as the evolution of massive stars. So far, stellar-mass BHs have been found to exist in binary systems termed X-ray binaries (XRBs; e.g., W. H. G. Lewin et al. 1995; J. van Paradijs 1995; R. A. Remillard & J. E. McClintock 2006). In our Galaxy, they have preferably been found in binary systems with a low-mass companion star, termed low-mass X-ray binaries (LMXBs; see E. Kalemci et al. 2022; A. Bahramian & N. Degenaar 2023, for detailed reviews). LMXBs are mostly X-ray transient sources, exhibiting bright, sporadic outbursts that typically last from months to years (e.g., R. A. Remillard & J. E. McClintock 2006; T. M. Belloni et al. 2011).

Currently, over 70 transient BH (candidate) XRBs have been identified.[36] Among these, about 20 contain a compact object confirmed to be in the BH mass range using dynamical methods, i.e., by measuring the orbital motion of their companion stars (J. M. Corral-Santana et al. 2016; A. Avakyan et al. 2023). Historically, these systems were predominantly discovered via capturing their transient outbursts by a series of wide-field X-ray monitoring instruments that have been flown since the 1970s, such as the Ariel-V (G. Villa et al. 1976), the all-sky monitor WATCH on board the Granat satellite (S. Brandt et al. 1990), the All-Sky Monitor on board the Rossi X-ray Timing Explorer (A. M. Levine et al. 1996), the INTErnational Gamma-Ray Astrophysics Laboratory (INTEGRAL; C. Winkler et al. 2003; E. Kuulkers et al. 2021), the Burst Alert Telescope (S. D. Barthelmy et al. 2005) on board the Neil Gehrels Swift Observatory (Swift; N. Gehrels et al. 2004), and the Monitor of All-sky X-ray Image (MAXI; M. Matsuoka et al. 2009). For the vast majority of these systems, the detected X-ray outbursts reached a peak luminosity typically over 10^{37} erg s^{-1} (e.g., Z. Yan & W. Yu 2015; B. E. Tetarenko et al. 2016), making them bright enough to be detected by most of the X-ray monitors mentioned above.

Only four BHs (candidates) were discovered by the detection of their X-ray emission during faint outbursts, with a peak luminosity $L_X \lesssim 10^{36}$ erg s^{-1} (R. Wijnands et al. 2006), namely, Swift J1357.2–0933 (J. M. Corral-Santana et al. 2013), XTE J1118+480 (R. M. Wagner et al. 2001), XTE J1728–295 (J. Swank & C. Markwardt 2001; R. Walter et al. 2004), and CXOGC J174540.0–290031 (M. P. Muno et al. 2005a; D. Porquet et al. 2005). The first two systems were

confirmed to harbor a BH through dynamical mass measurements, while the latter two were well consistent with BH transients in their observed properties. The small number of BHs found during faint outbursts can be explained in the sense that the peak X-ray brightnesses of the majority of such systems fall below the sensitivity of the past and most current wide-field monitors, while the sensitive X-ray telescopes (such as Chandra and XMM-Newton) have too small field of view (FOV) to catch the outbursts in real time (the case of CXOGC J174540.0–290031 is an exception, and the chance of such detections is expected to be low).

It has long been recognized that the number of BH XRBs (BHXRBs) known so far is much smaller than what was hypothesized to exist in our Galaxy (E. P. J. van den Heuvel 1992). Based on the distances and spatial distributions of the known BHXRBs, it was estimated that there are more than 10^3 BHXRBs in our Galaxy (J. M. Corral-Santana et al. 2016). In fact, stellar evolution models predicted that there could be as many as 10^8–10^9 BHs lurking in our Galaxy (e.g., G. E. Brown & H. A. Bethe 1994; F. X. Timmes et al. 1996; D. L. Meier 2012). This "missing" population of stellar-mass BHs has been a topic of extensive debate for decades (C. J. Hailey et al. 2018). The apparently very low detectability of BHXRBs is likely attributable to their presumably transient nature and the fact that most of their outbursts are likely too faint to be detectable by the past and most of the current X-ray wide-field monitors. It is thus expected that, with the advent of X-ray wide-field monitors having significantly improved sensitivity, more of such systems could be revealed. Nonetheless, further challenges lie with the identification of the nature of the compact object (be it a BH or a neutron star (NS)) for LMXBs, which requires dense monitoring and prompt multiwavelength follow-up observations (R. Wijnands et al. 2006; A. Bahramian & N. Degenaar 2023).

The Einstein Probe (EP; W. Yuan et al. 2022), launched on 2024 January 9, carries the Wide-field X-ray Telescope (WXT)—a wide-field monitor with an FOV of $\sim$3800 deg^2 built from lobster-eye micropore optics. Operating in the 0.5–4 keV band, WXT can reach a sensitivity of $\sim$1 mcrab ($\sim$(2–3) $\times 10^{-11}$ erg s^{-1} cm^{-2} in 0.5–4 keV) at an exposure of $\sim$1000 s, which is a factor of several tens more sensitive than the other currently operating wide-field monitors. For BHXRBs within our Galaxy, an X-ray outburst brighter than $\sim$$10^{35}$ erg s^{-1} will likely be detected by WXT within $\sim$$10^3$ s, enabling the detection of outbursts that are $\sim$100 times fainter than those previously detectable. The other instrument on board EP is the Follow-up X-ray Telescope (FXT; Y. Chen et al. 2020) operating in the 0.3–10 keV band, which provides source localization of 5″–10″ and sensitivity of $\sim$$10^{-14}$ erg s^{-1} cm^{-2} at an exposure of 10^4 s. It is expected that EP will detect new BHXRB systems, particularly those undergoing faint, short-lived outbursts (W. Yuan et al. 2025).

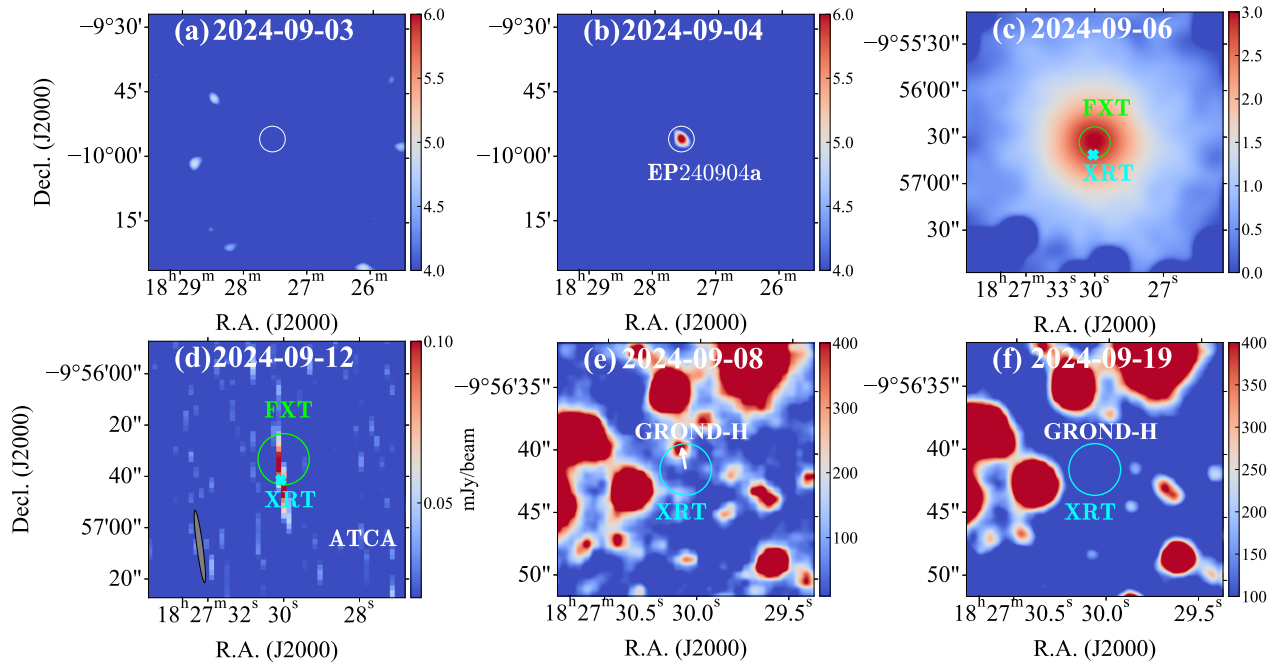[36] https://www.astro.puc.cl/BlackCAT/transients.php

Figure 1. Panels (a) and (b) show EP/WXT images of EP J182730.0−095633 from 2024 September 3 to 4 (ObsIDs are 06800000068 and 06800000067, respectively). Panel (c) presents EP/FXTA image obtained with FF mode on 2024 September 6. Panel (d) displays ATCA (5.5 GHz) images on 2024 September 12. The restoring beam ($19\overset{''}{.}5 \times 1\overset{''}{.}2$, $5\overset{\circ}{.}5$) is indicated as a gray elliptical shape in the lower left corner. Panels (e) and (f) show NIR (*H*-band) images obtained from GROND on 2024 September 8 and 19, respectively. The potential NIR counterpart is denoted by the white arrow in panel (e). The white, green, and cyan circles represent the positional errors of WXT, FXT, and XRT, respectively.

In this Letter, we report on the discovery and multi-wavelength follow-up observations of X-ray transient EP J182730.0−095633 (EP240904a; H. Q. Cheng et al. 2024b) located on the Galactic plane. The spectral, temporal, and multiwavelength properties observed favor this source being a new BHXRB candidate experiencing a faint outburst lasting for about 20 days. This Letter is organized as follows: In Section 2, we describe the observations and data reduction procedures. The results are presented in Section 3 and discussed in Section 4. The conclusion is given in Section 5.

2. Observations and Data Reduction

2.1. X-Ray

EP J182730.0−095633 was first detected as an X-ray transient (designated EP240904a) in an observation starting on 2024 September 4 at 10:12:56 UT by EP/WXT (H. Q. Cheng et al. 2024b). The source was not detected during a WXT observation taken 1 day before (Figure 1). Following the detection of the source, a series of follow-up observations were carried out with EP/FXT starting on 2024 September 6 and lasting until September 24. These observations provided a more precise source position at R.A. (J2000.0) = $18^{h}27^{m}30\overset{s}{.}0$ and decl. (J2000.0) = $-9°56'33''$, with an uncertainty of $10''$ at the 90% confidence level (H. Q. Cheng et al. 2024b). Meanwhile, several other X-ray telescopes were triggered and joined the follow-up campaign, including Swift, the Neutron Star Interior Composition Explorer (NICER; K. C. Gendreau et al. 2016), the Nuclear Spectroscopic Telescope Array (NuSTAR; F. A. Harrison et al. 2013), and the Hard X-ray Modulation Telescope (Insight-HXMT; S.-N. Zhang et al. 2020).[37] The X-ray Telescope (XRT) aboard

Swift provided an enhanced positional accuracy (P. A. Evans et al. 2009, 2020), by applying a correction based on the photometry provided by the Ultra-Violet/Optical Telescope (UVOT): R.A. (J2000.0) = $18^{h}27^{m}30\overset{s}{.}1$ and decl. (J2000.0) = $-9°56'41\overset{''}{.}4$, with an uncertainty of $2\overset{''}{.}1$ at the 90% confidence level. For this work, we adopt the Swift/XRT coordinates as the X-ray position of EP J182730.0−095633. It is important to point out that EP J182730.0−095633 resides on the Galactic plane ($l = 21\overset{\circ}{.}3634$, $b = 0\overset{\circ}{.}7244$), suggesting a likely Galactic origin for this transient. The observation log is summarized in Table B1, and the data reduction process is detailed in Appendix A.1.

2.2. Optical and Infrared

Follow-up observations of EP J182730.0–095633 were carried out in the optical and near-infrared (NIR) bands with various ground- and space-based telescopes. These include the Thai Robotic Telescope (TRT), the Nordic Optical Telescope (NOT), the Altay 1-Meter Telescope (ALT100C), the Visible Telescope (VT) on board the Space-based multiband astronomical Variable Objects Monitor (SVOM), the Tsinghua-NAOC Telescope (TNT; F. Huang et al. 2012) in Xinglong Observatory, the Multi-channel Photometric Survey Telescope (Mephisto; X. Yuan et al. 2020) and the Gamma-Ray Burst Optical/Near-Infrared Detector (GROND; J. Greiner et al. 2008) at the Max Planck Society for the Advancement of Science (MPG) 2.2 m telescope at European Southern Observatory (ESO)'s La Silla Observatory. The observational log is listed in Table B2 and the data reduction of these observations is detailed in Section A.3.

2.3. Radio

Follow-up observations of EP J182730.0–095633 were conducted in the radio band with two ground telescopes, the

---

[37] Due to contamination from nearby sources, data from Insight-HXMT were excluded from further analysis.

Australia Telescope Compact Array (ATCA) and MeerKAT (F. Camilo et al. 2018; J. Jonas 2018). Two ATCA observations were carried out on September 12 (A. Wang et al. 2024a) and 2024 September 21. MeerKAT observed the source for three times, on 2024 September 21, October 21, and October 28. The observational log is listed in Table B3, and the data reduction of these observations is detailed in Section A.4.

3. Data Analysis and Results

3.1. X-Ray Spectral Analysis

The X-ray spectral analysis was performed using XSPEC v12.14.0b (K. A. Arnaud 1996), based on data collected after September 4 from EP/WXT, EP/FXT, NICER, Swift, and NuSTAR. The energy bands used for spectral fitting were 0.5–4 keV (EP/WXT), 0.5–10 keV (EP/FXT), 0.5–10 keV (NICER), 0.3–10 keV (Swift), and 4–79 keV (NuSTAR). The Swift, NICER, NuSTAR, and EP/FXT spectra before September 20 were grouped with a minimum of 25 counts bin^{-1}, and the best fit was determined by minimizing the χ^2 statistic. The EP/FXT spectra after September 20 and the EP/WXT spectra, due to the lower number of counts, were grouped with a minimum of 2 counts bin^{-1}, and the best fit was obtained by minimizing the Cash statistic (W. Cash 1979). All uncertainties are reported at the 90% confidence level for a single parameter of interest unless otherwise stated.

We began the spectral fitting using a simple absorbed power-law model (tbabs*powerlaw in XSPEC). The abundances were set to WILM (J. Wilms et al. 2000), and the cross sections were set to VERN (D. A. Verner et al. 1996). In most cases, all parameters, including the column density $N_{\rm H}$, the photon index Γ, and the normalization, are allowed to vary. However, due to the low spectral quality of the WXT observations from September 4 to 6 and the FXT observations after September 20, $N_{\rm H}$ could not be constrained within physically meaningful ranges. Therefore, we fixed $N_{\rm H}$ at $3.1 \times 10^{22}\,{\rm cm}^{-2}$, derived from the FXT observation on September 6, which offered the best spectral quality. A simple absorbed power-law model yields acceptable fits for all spectra. The fitted parameters are summarized in Table B1. We also tested the spectral fitting with the blackbody (tbabs*bbodyrad) or disk blackbody (tbabs*diskbb) model. However, neither of them provides a satisfactory fit. In addition, we performed a joint spectral fitting using the simultaneous EP/FXT and NuSTAR observations taken on September 11. A Constant model was applied to correct for calibration differences between different telescopes, with NuSTAR/FPMA fixed at unity as the reference. Across the wide energy range of 0.5–79 keV, the spectra are still represented by the absorbed power-law model, with no evidence of iron line signatures and thermal contributions, resulting in a fit statistic of χ^2/dof = 1002.40/1011 and a photon index of 1.91 ± 0.01. On this basis, although the powerlaw model has already provided a statistically acceptable fit, we further tentatively test the fits and estimate the high-energy cutoff by replacing the powerlaw model with two models, cutoffpl (refer to Figure 2 for an example) and nthcomp (A. A. Zdziarski et al. 1996; P. T. Życki et al. 1999), respectively. Both models provide an equivalently acceptable fit compared with that of the powerlaw model. For the former, the cutoff energy is larger than 200 keV. The nthcomp model, on the other hand, yields
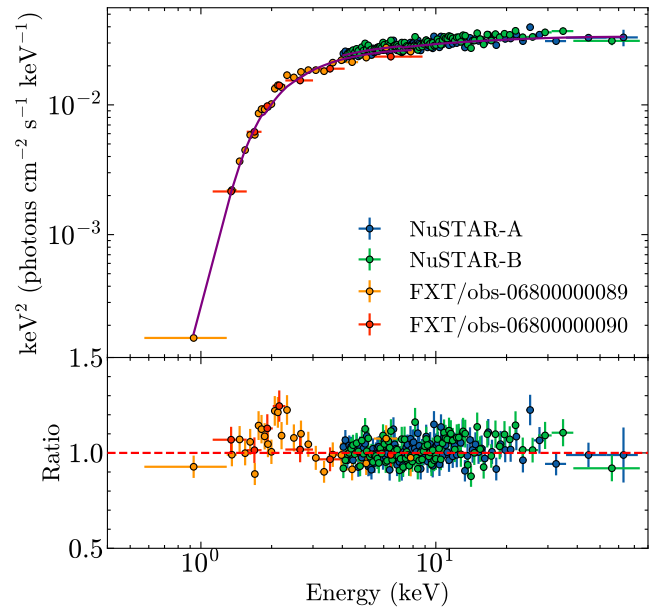

Figure 2. Joint spectral fitting of EP/FXT (module B, 0.5–10 keV) and NuSTAR (4–79 keV) with an absorbed cutoff power-law model. Note that the residual feature at ~2 keV is due to a calibration issue.

a stringent constraint of $T_e > 30\,{\rm keV}$, with the blackbody temperature parameter inherent in this model fixed at a typical value of 0.1 keV. In both cases, the best-fitting column density and photon index are consistent with those obtained using the simple absorbed power-law model. In short, we conclude that the X-ray spectrum of EP J182730.0–095633 is dominated by nonthermal emission.

The unabsorbed source flux in the 0.5–10 keV band is calculated using the cflux model in XSPEC. To determine the upper limit of the preoutburst X-ray brightness, we stack the WXT data from September 1 to 3, utilizing the same source extraction and background regions as for the real detection observations. The count rate is then converted to flux using the factor derived from the first WXT detection, under the assumption that the spectral shape remained stable during the rising phase of the outburst. It is worth noting that while this assumption may not be entirely physically justified, the main conclusions should remain unaffected. At the end of the outburst, the source was not detected in the second Swift/XRT observation. We determine the upper limit of the count rate from the 0.5–10 keV image and then evaluate the postoutburst flux using the WEBPIMMS tool[38] with assumptions of $N_{\rm H} = 3.1 \times 10^{22}\,{\rm cm}^{-2}$ and $\Gamma = 2.0$, representing the typical spectral parameters during the outburst.

3.2. X-Ray Temporal Analysis

3.2.1. Long-term X-Ray Behavior

In Figure 3, we present the long-term evolutionary trend of X-ray flux, Γ, and $N_{\rm H}$ during the outburst. The full outburst lasted approximately 3 weeks, during which the source's flux varied by more than three orders of magnitude. Following a rapid rise to a peak flux of approximately $5.2 \times 10^{-10}\,{\rm erg\,s}^{-1}\,{\rm cm}^{-2}$ on September 5, the flux gradually decreased to a minimum of $\sim 2 \times 10^{-13}\,{\rm erg\,s}^{-1}\,{\rm cm}^{-2}$ on September 24. The decline phase

---

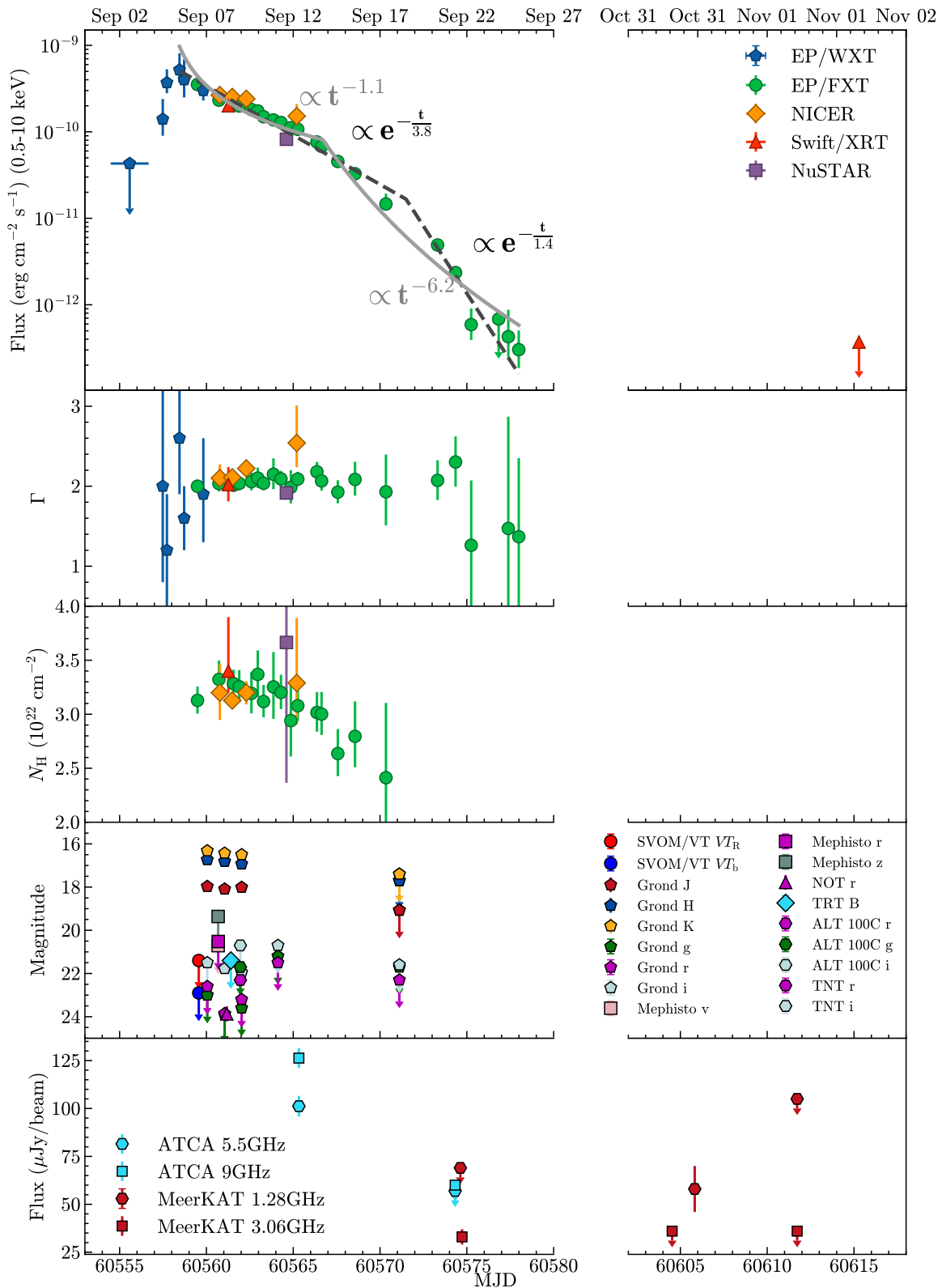[38] https://heasarc.gsfc.nasa.gov/cgi-bin/Tools/w3pimms/w3pimms.pl

Figure 3. Long-term evolution of the multiwavelength properties of EP J182730.0–095633. Top to bottom: the evolutions of the unabsorbed flux in the 0.5–10 keV band, the photon index (Γ), the hydrogen column density ($N_{\rm H}$), the observed magnitude in the optical/infrared bands, and the radio peak flux density of ATCA and MeerKAT. The X-ray flux during the decaying phase is fitted by either a broken power-law model (gray solid curve) or a broken exponential model (black dashed curve). See Section 3.2.1 for more details. The results of a few optical/infrared observations after the X-ray outburst, where only upper limits have been obtained, are not shown for clearer data visualization. In addition, primarily due to the low signal-to-noise ratio of the data, the X-ray absorbing column density $N_{\rm H}$ in some observations cannot be well constrained within physically reasonable ranges and are fixed at 3.1×10^{22} cm^{-2}; hence, they are not shown in this figure (see text and Table B1 for more details).

Figure 4. Power density spectra of the EP/FXTA data (left panel; ObsID 06800000091) and NuSTAR data (right panel; ObsID 91001334002), with the bottom of each panel showing the power ratio between the data and best-fitting bending power-law model.

displays a two-stage pattern. When employing a broken power-law model to fit the long-term light curve, there is an initial slow decay of $t^{-1.1}$ transitioning to a more rapid drop of $t^{-6.2}$, occurring 9.3 days after the source's discovery. Alternatively, when using a broken exponential decay model, which provides a better fit, a transition is observed at 14.1 days. Prior to this transition, the flux decreases at a rate of $e^{-\frac{t/1\,\mathrm{day}}{3.8}}$, which accelerates to $e^{-\frac{t/1\,\mathrm{day}}{1.4}}$ after the break. This dual decay pattern might correspond to different underlying physical mechanisms.

Although there are evident changes in the source's brightness, Γ remains fairly stable, exhibiting a consistent value of ~ 2 throughout the outburst. On the other hand, the column density N_{H} slightly decreases from $\sim 3 \times 10^{22}\,\mathrm{cm}^{-2}$ to $\sim 2 \times 10^{22}\,\mathrm{cm}^{-2}$ between September 6 and 17, suggesting that the origin of X-ray absorption is intrinsic to the source. The observed excess above the Galactic H I column density in the direction of the source, which is around $1.13 \times 10^{22}\,\mathrm{cm}^{-2}$ as determined using the HI4PI Survey map (HI4PI Collaboration et al. 2016) accessed through the HEASARC online tool,[39] also supports this interpretation. We also calculated the evolutionary trend of the spectral index while keeping the column density fixed at the typical value of $3.1 \times 10^{22}\,\mathrm{cm}^{-2}$, yielding results consistent with those presented above within measurement uncertainties (see Figure B1 for an illustration).

3.2.2. Short Timescale Variability

We conducted a search for thermonuclear X-ray bursts and pulsations in all available X-ray data, as these phenomena serve as strong evidence for identifying the source in an NS system. However, no thermonuclear X-ray bursts were identified in the light curves. Additionally, no significant pulsations were detected in the power spectra, with 3σ upper limits on the flux pulsed fraction of 6%–10% for the second NICER observation, 8%–13% for the NuSTAR observation, and 6%–13% for the EP/FXT observations across the frequency range 30–1000 Hz (for more details, see Appendix A.2). Although the light curves

do not show thermonuclear X-ray bursts or pulsations, they present strong short-time variations. We conducted a power spectral density (PSD) analysis using a timing resolution of 0.1 s and a segment length of 256 s or 512 s. For most observations a segment length of 512 s is adopted, while for observations with relatively short good time intervals (GTIs) a 256 s segment length is chosen for a higher signal-to-noise ratio in the resulting PSD. The PSD is normalized in units of rms^2 Hz^{-1} (T. Belloni & G. Hasinger 1990). Figure 4 displays the PSDs for the observations taken by EP/FXT module A (FXTA) and NuSTAR/FPMA. The continuum component of both PSDs exhibits increased noise toward lower frequencies (red noise) and can be well modeled by a bending power-law function with a break frequency of around 0.03–0.06 Hz. Additionally, there is a prominent, narrow peak around 0.038 Hz, indicating the presence of a quasiperiodic oscillation (QPO) with an rms amplitude of $\sim 20\%$. To assess the significance of the QPO, we simulated 100,000 light curves, based on the method of J. Timmer & M. König (1995) from the best-fit bending power-law PSD. We then calculated the PSDs of these light curves and determined the distribution of the variability power at each Fourier frequency. The significance of the QPO greatly exceeds the 3σ confidence threshold, with the quality factor $q \equiv \nu_0/(2\Delta\nu)$ estimated to be $\gtrsim 8$. The QPO is also present in the FXT module B (FXTB) data, collected in the Partial Window (PW) mode, with a centroid frequency, significance, and q-factor that roughly match those found in the FXTA data. The QPO feature is evident in other FXT observations before September 20, as shown in Figure B2, with the centroid frequency remaining around 0.04 Hz despite the X-ray flux varying by more than two orders of magnitude. After September 20, no clear QPO signal was observed, probably because of the very low count rate of the source. In addition, a similar QPO is also detected in the NICER data, although with lower significance of about 2σ (Figure B2).

3.3. Optical and Infrared Detection

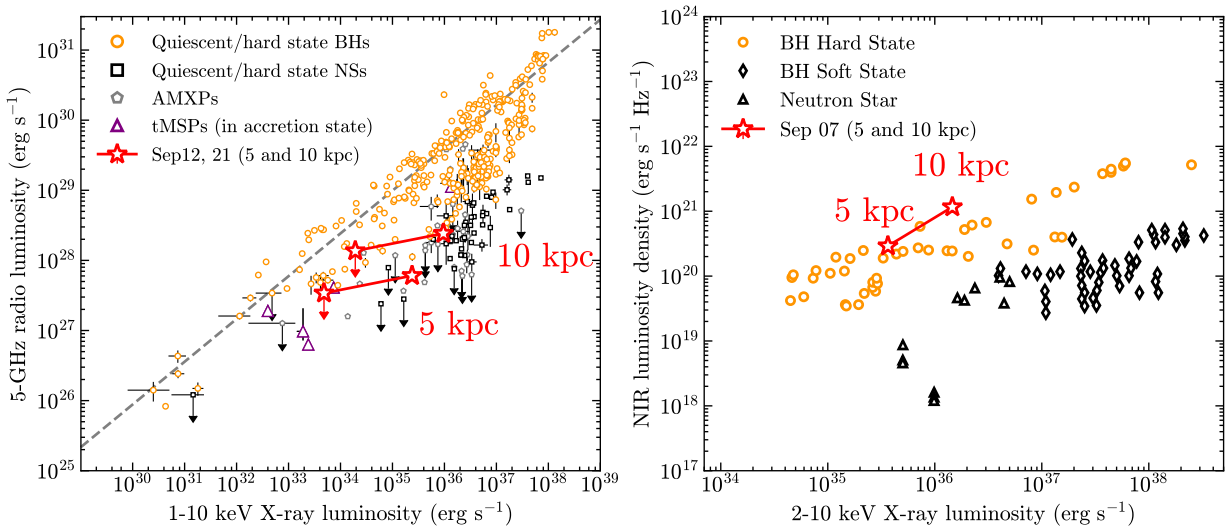SVOM/VT rapidly responded to observe the field of EP J182730.0–095633 on September 6, yet no uncataloged objects

---

Figure 5. Quasi-simultaneous X-ray vs. radio and NIR luminosities for LMXBs, including EP J182730.0−095633. Left: the radio–X-ray (L_{Radio}–L_X) fundamental plane for XRBs, adopted from A. Bahramian & A. Rushton (2022). The results of EP J182730.0−095633 are represented by red symbols, assuming various distance values. Right: the position of EP J182730.0−095633 on the NIR–X-ray ($L_{NIR(JHK)}$–L_X) correlation for XRBs (D. M. Russell et al. 2006). The data are taken on September 7 (the results barely change for those of September 8 and 9) and corrected for absorption using extinction values of $A_H = 2.8 \pm 0.1$ mag. For brevity, only the results of the H band are displayed here as a representative, with similar results for the other two bands.

were detected within the Swift/XRT error circle. The 5σ upper limits for the VT_R (650–1000 nm) and VT_B (400–650 nm) bands are 21.4 and 22.9 mag, respectively. From September 7 to 9, this field was extensively observed by several instruments, including GROND, NOT, Mephisto, TRT, and ALT100C. The observations of Mephisto, TRT, and ALT100C did not uncover any new or flaring objects around the X-ray position, but an uncataloged source was detected by GROND in the NIR J, H, and K_s bands in all three epochs (see panels (e) and (f) in Figure 1), with consistent magnitudes of $J \sim 18$ mag, $H \sim 16.8$ mag, and $K_s \sim 16.4$ mag, all in the AB system (see Table B2). The position of the NIR signal is R.A. = $18^h27^m30^s.09 \pm 0^s.01$ and decl. = $-9°56'39.6'' \pm 0.2''$. It is worth noting that the signal was also marginally detected by NOT in the r band on September 7 (with a magnitude of 23.87 ± 0.35 mag; S. Y. Fu et al. 2024), as well as by GROND in both r' and i' bands on September 8 (with magnitudes of 23.86 ± 0.30 mag and 21.77 ± 0.10 mag, respectively). Interestingly, this source was no longer detected in the following GROND observations carried out on September 11 and thereafter, clearly indicating a fading behavior. Additionally, at the end of the X-ray outburst, SVOM/VT and TNT carried out two additional observations for this field on September 28 and October 11, respectively, yet no sources were detected. The long-term evolution of the apparent magnitudes during the X-ray outburst is shown in the bottom panel of Figure 3.

The faint optical and NIR detection is likely due to high extinction, given the low Galactic latitude of EP J182730.0–095633. Specifically, in the source direction the Galactic foreground reddening in the V band is very severe, with $A_V \sim 15.4$–15.8 mag (E. F. Schlafly & D. P. Finkbeiner 2011) accessed through dust extinction tools on the NASA/IPAC Extragalactic Database[40] and IRAS.[41] The reddenings for the GROND J and H bands are estimated to be 4.4 ± 0.1 mag and 2.8 ± 0.1 mag, respectively, by

applying the relationship between A_λ and A_V taken from J. A. Cardelli et al. (1989). We take these values for subsequent NIR luminosity calculations (see Section 4). The results of GROND and EP/FXT observations during the source detections by GROND from September 7 to 9 were taken for the investigation of the L_X–L_{NIR} correlation, as shown in the right panel of Figure 5.

3.4. Radio Detection

The first ATCA observation on September 12 identified a radio source at the X-ray position (Figure 1). At 5.5 GHz the source position was R.A. = $18^h27^m30^s.16 \pm 0^s.39$ and decl. = $-9°56'36.''0 \pm 3.''51$, while at 9 GHz it was located at R.A. = $18^h27^m30^s.07 \pm 0^s.21$ and decl. = $-9°56'40.''4 \pm 2.''09$. The radio locations are $5.''4 \pm 4.''1$ and $1.''0 \pm 3.''0$ away from the Swift X-ray position, respectively. The peak flux densities at 5.5 and 9 GHz were measured to be $101.2 \pm 5.4 \,\mu$Jy beam^{-1} and $126.3 \pm 5.2 \,\mu$Jy beam^{-1}, respectively. The radio spectral index (α) is 0.45 ± 0.14, showing an inverted spectrum. During a subsequent ATCA observation, conducted on September 21, no significant radio emission was detected, yielding 3σ upper limits of $57 \,\mu$Jy beam^{-1} at 5.5 GHz and $60 \,\mu$Jy beam^{-1} at 9 GHz. A slight positional offset ($\sim 4.''5$) was observed between the centroids at the two frequencies in the first ATCA observation, with a significance level of 3σ. It remains unclear whether this discrepancy is due to intrinsic physical processes or systematic errors from instrumental effects, as the source was undetectable in later observations. The results of EP/FXT and ATCA observations on September 12 and 21 were taken for the investigation of the L_X–L_{Radio} correlation, as shown in the left panel of Figure 5.

In the first MeerKAT epoch we obtained a detection at S band (3.06 GHz) in which the source is located at R.A. = $18^h27^m30^s.00 \pm 0^s.009$ and decl. = $-9°56'39.''75 \pm 0.''13$, with a flux density of $33 \pm 4 \,\mu$Jy, while at L band (1.28 GHz) we have a nondetection, with a 3σ upper limit of $69 \,\mu$Jy beam^{-1}. The source position obtained by MeerKAT is consistent with those provided by Swift/XRT and ATCA at 9 GHz. The spectral shape

---

of MeerKAT is also consistent with the positive spectral index obtained in the first ATCA epoch. In our second MeerKAT epoch we obtain a detection at L band at $58 \pm 12\,\mu$Jy and a nondetection at S band with a $36\,\mu$Jy beam^{-1} 3σ upper limit. Finally, we obtained no detections at both L band and S band in our third MeerKAT epoch, with 105 and $36\,\mu$Jy beam^{-1} upper limits, respectively. The results of ATCA and MeerKAT are summarized in Table B3.

4. Discussion

4.1. Nature of the Transient

EP J182730.0–095633 (EP240904a) is a new X-ray transient discovered by EP/WXT on 2024 September 4. Follow-up observations were performed with multiple X-ray telescopes and multiwavelength facilities. In this Letter, we report on the spectral and temporal properties of this source during the outburst, aiming to uncover its physical nature.

At the corresponding location of EP J182730.0–095633, a faint NIR transient source was detected by GROND and NOT. The NIR flux showed a rapid decay and became undetectable within a few days, accompanied by a simultaneous decline in the X-ray flux. Given its spatial and temporal coincidence, we suggest that the transient source detected by GROND and NOT is very likely to be associated with EP J182730.0–095633, thus representing a promising candidate for the NIR counterpart. We note that the nondetection of the signal in optical bands can be attributed to the large Galactic foreground reddening of $A_V \approx 15.4$–15.8 mag along the line of sight.

Due to the faintness and rapid diminishing of the potential counterpart, no optical/NIR spectrum was obtained, and thus no redshift measurement could be made. The absence of a redshift measurement complicates the task of determining the source's nature. However, it is largely unlikely that this transient is either a gamma-ray burst (GRB) or a stellar flare, due to the differing characteristics. GRBs generally exhibit a much shorter timescale for their rise and decay, with the former typically occurring within a few seconds and the latter lasting a few days (B. Zhang et al. 2006), whereas stellar flares are characterized by X-ray spectra primarily described by one or several optically thin thermal plasma components (A. O. Benz & M. Güdel 2010).

The tidal disruption event (TDE) may be a potential scenario, given that some of the observational properties of EP J182730.0–095633, such as the nonthermal X-ray spectrum, two-stage decaying trend, and radio and infrared detections, are broadly consistent with a rare class of TDEs dominated by a relativistic jet (e.g., J. S. Bloom et al. 2011; D. N. Burrows et al. 2011; D. R. Pasham et al. 2015). However, the infrared-to-X-ray flux ratio appears to be significantly higher compared to that observed in jetted TDEs (e.g., D. R. Pasham et al. 2015; A. J. Levan et al. 2016). Meanwhile, we do not observe a plateau phase or strong intraday variability in X-rays, which instead are common features in those jet-dominated systems. Therefore, the possibility of EP J182730.0–095633 being a jetted TDE seems less unlikely. Moreover, it is interesting to point out that, despite numerous differences, EP J182730.0–095633 has exhibited a PSD profile similar to a rare white dwarf–terrestrial icy planet TDE candidate IGR J17361–4441 (E. Bozzo et al. 2011; M. Del Santo et al. 2014) discovered by the IBIS/ISGRI telescope (P. Ubertini et al. 2003) on board INTEGRAL on

2011 August 11, which shows a notable QPO signal with a centroid frequency of $\sim$100 mHz (E. Bozzo et al. 2014).

In contrast, EP J182730.0–095633 resembles XRBs in a variety of aspects regarding the source position, radio emission, X-ray variability, spectral properties, and multiwavelength relationships. First, the position of EP J182730.0-095633 is on the Galactic plane, a region densely populated by XRBs (e.g., H. J. Grimm et al. 2002; A. Bahramian & N. Degenaar 2023). Second, the X-ray flux of EP J182730.0–095633 generally follows a fast-rise-exponential-decay (FRED) behavior, which agrees largely with the canonical outburst behavior of XRBs (W. Chen et al. 1997; R. A. Remillard & J. E. McClintock 2006). The multifold pattern during the decaying phase can also be interpreted within the context of XRB outbursts (e.g., A. R. King & H. Ritter 1998; G. Dubus et al. 2001; S.-S. Weng & S.-N. Zhang 2015). Third, as shown in Figure 5, EP J182730.0–095633's positions on the L_X–L_{Radio} and L_X–L_{NIR} diagrams are in good agreement with an XRB origin, assuming a distance of several kiloparsecs. Additionally, the radio detection, combined with an inverted radio spectrum obtained by ATCA and MeerKAT, may suggest the presence of a compact jet, which is commonly observed in the hard states of XRBs (see T. Belloni 2010, and references therein). This possibility is further supported by the observed nonthermal power-law spectrum, a characteristic feature in the hard states. The spectral shape variation in the radio band during the late outburst stage implies that the compact jet transitioned from an optically thick to optically thin state (see Section 3.4), a phenomenon commonly observed during the decay phase of XRB outbursts (e.g., S. Corbel et al. 2013; M. Díaz Trigo et al. 2018). More importantly, the QPO signal, which is a prevalent feature in XRBs (A. R. Ingram & S. E. Motta 2019), is significantly detected during a long period of the outburst.

4.2. Properties of the Accreting System

If EP J182730.0−095633 is a Galactic XRB, the peak X-ray luminosity ($L_{2-10\,keV}$) is estimated to be $\lesssim 10^{36}$ erg s^{-1}, assuming a distance of several kiloparsecs. According to R. Wijnands et al. (2006), it can then be classified as a borderline faint to very faint XRB (VFXB). These sources were recently and extensively discovered in the Galactic center, Galactic plane, and Galactic bulge by ASCA, Swift, Chandra and XMM-Newton surveys (e.g., A. D. P. Hands et al. 2004; M. P. Muno et al. 2005a, 2005b; M. Sakano et al. 2005; N. Degenaar & R. Wijnands 2009; for a detailed review, one may refer to A. Bahramian & N. Degenaar 2023). Their outbursts typically last for several weeks to months (e.g., N. Degenaar & R. Wijnands 2009; C. O. Heinke et al. 2015; S.-S. Weng & S.-N. Zhang 2015).

Identifying the nature of the central compact object (NS or BH) is somehow challenging for EP J182730.0–095633, due primarily to the lack of definitive evidence supporting either scenario (e.g., coherent pulsations, thermonuclear bursts, or dynamical mass estimation). Its locations on the radio versus X-ray luminosity fundamental plane (see left panel of Figure 5) fall onto the overlapping regions of BHs and NSs, yielding an inconclusive argument. Nevertheless, we are inclined to argue that EP J182730.0–095633 is more likely to be a BHXRB for the following reasons. First, the X-ray emission throughout the outburst is consistently described by a nonthermal power-law spectrum with a photon index maintaining at $\sim$2. This "stable" behavior largely precludes the

source being an NS accreting system, as the spectrum of the latter often exhibits a softening trend as the luminosity decreases below $10^{36} \, \mathrm{erg \, s^{-1}}$ owing to the presence and growing prominence of the NS surface emission (R. Wijnands et al. 2015). This dichotomy in the spectral shape evolution has been increasingly studied in recent years (e.g., R. M. Plotkin et al. 2013; R. Wijnands et al. 2015; E. Qiao & B. F. Liu 2020) and developed to be a diagnostic tool for identifying (candidate) BHs (e.g., M. Stoop et al. 2021). Second, the relative strength of the X-ray and NIR emissions (Figure 5) closely aligns with those typically observed in BH binaries in the hard state (D. M. Russell et al. 2006). Third, the joint spectral fitting of EP/FXT+NuSTAR data indicates a relatively high electron temperature of $T_e > 30$ keV (see Section 3.1), which is more prone to exist in BH systems (e.g., M. J. Burke et al. 2017; S. Banerjee et al. 2020). Furthermore, even though mHz QPOs are detected in a number of NS systems and are usually attributed to the marginally stable nuclear burning on the NS surface (e.g., M. Revnivtsev et al. 2001; T. E. Strohmayer & E. A. Smith 2011; G. C. Mancuso et al. 2019; M. Lyu et al. 2020; G. C. Mancuso et al. 2023; K. Tse et al. 2023), the only two VFXBs with QPO detection, Swift J1357.2–933 (M. Armas Padilla et al. 2014; A. Beri et al. 2023) and XTE J1118+480 (M. Revnivtsev et al. 2000; K. S. Wood et al. 2000), have been confirmed to host BH accretors. Future observations, particularly dynamical mass measurements, are essential to verify this scenario and unveil the mysterious nature of EP J182730.0–095633.

Regarding the companion star, its nature remains largely inconclusive owing to the current lack of spectroscopic information. However, we can tentatively explore this issue based on the quasi-quiescent NIR luminosity, assuming that it is contributed mainly by the companion. Specifically, considering the upper limit of $m_J > 19.2$ mag given by GROND observations on September 18 (near the end of the X-ray outburst), the corresponding absolute magnitude upper limit is $M_J > 4.7$ mag assuming a distance of 10 kpc and a Galactic foreground dust extinction of $A_J = 4.4$ mag. According to typical stellar parameters (M. J. Pecaut et al. 2012; M. J. Pecaut & E. E. Mamajek 2013), the companion star is likely a late-type K/M star, indicating that this source is a potential LMXB.

The X-ray outburst of EP J182730.0–095633 resembles the "hard-only" outbursts widely observed in XRBs (e.g., Z. Yan & W. Yu 2015; B. E. Tetarenko et al. 2016; K. Alabarta et al. 2021), which are notably characterized by the absence of state transitions. Its X-ray spectra show no iron Kα line or thermal component, indicating that the standard Shakura–Sunyaev disk (N. I. Shakura & R. A. Sunyaev 1973) is either absent or truncated at a large radius. The accretion close to the compact object is likely to operate in the form of an optically thin, geometrically thick advection-dominated accretion flow (S. Ichimaru 1977; R. Narayan & I. Yi 1994, 1995b, 1995a; F. Yuan & R. Narayan 2014). The observed X-ray spectral index remains relatively constant throughout the entire outburst, suggesting that the geometry of the accretion flow is relatively stable during the flaring activity. In such a scenario, the mHz QPOs, potentially generated by Lense–Thirring precession or quasiperiodic obscurations (as discussed in A. Beri et al. 2023), could exhibit stable frequencies, as observed.

We also note that there is another possibility that EP J182730.0–095633 is an extragalactic XRB system. If the correlation between X-ray and radio emissions is expected to follow the $L_X–L_{Radio}$ relation typical of XRBs, its estimated distance would be within $\sim 10^2$ kpc. However, there are no nearby satellite galaxies in the direction of EP J182730.0–095633 (A. Drlica-Wagner et al. 2020), making this scenario less likely.

4.3. mHz QPO Signal

Despite the ubiquitous nature of QPOs in BHXRBs across various spectral states, the detection of the mHz QPO remains relatively rare (A. R. Ingram & S. E. Motta 2019), with only a few cases reported in the past few years (MAXI J1820+070, Y. Li et al. 2025; H1743–322, D. Altamirano & T. Strohmayer 2012; MAXI J1348–630, X.-L. Wang et al. 2024b). The centroid frequency of the mHz QPO falls within the range of type C low-frequency QPOs (LFQPOs), the most common type of QPO in XRBs (e.g., S. Motta et al. 2011; D. J. K. Buisson et al. 2019). To tentatively probe the association of this ~ 40 mHz QPO signal with the commonly observed type C QPOs, we calculate the fractional-rms spectrum of QPOs using the data of EP-FXT and NuSTAR obtained on 2024 September 11, as shown in the left panel of Figure B3. Regardless of a large uncertainty, the rms-energy spectrum exhibits an enhanced fractional variability with the increasing photon energy below ~ 20 keV and then tends to flatten toward higher energies. This is generally consistent with that observed in type C LFQPOs of XRBs (e.g., P. Casella et al. 2004; J. Rodriguez et al. 2004; J. S. Yadav et al. 2016; Z.-X. Yang et al. 2024). We further calculate the relation between the QPO frequency and the low-frequency PSD break for QPO detections with significance exceeding 3σ, as presented in the right panel of Figure B3. The measurement of the EP transient is denoted with blue circles, and the canonical W–K relation built for type C LFQPOs (R. Wijnands & M. van der Klis 1999) is signified with a black dashed line. Notably, the mHz QPO of EP J182730.0–095633 exhibits a much lower centroid frequency than predicted by the empirical W–K relation, and also the QPO frequency remains quite stable despite the variations in the PSD break. This makes it much less likely to be a typical type C QPO. In this context, the QPO detected in EP J182730.0–095633 may represent a new class of LFQPOs in BHXRBs. It is also interesting to point out that the relative position of break and QPO looks similar to the LFQPOs found in some ultraluminous X-ray sources (e.g., G. C. Dewangan et al. 2006; K. Atapin et al. 2019; H. El Byad et al. 2025). We note that a detailed investigation on the origin of this ~ 40 mHz QPO is beyond the scope of this Letter and will be deferred to future work.

5. Conclusions

In this Letter, we report on the discovery and multiwavelength follow-up observations of an intriguing X-ray transient, EP J182730.0–095633 (EP240904a). This transient was first detected by EP/WXT on 2024 September 4, with its location on the Galactic plane ($l = 21°.3634$, $b = 0°.7244$). The source underwent a faint ($F_{\mathrm{peak}, 0.5-10 \, \mathrm{keV}} \approx 5.2 \times 10^{-10} \, \mathrm{erg \, s^{-1} \, cm^{-2}}$), short-lived ($\sim 20$ days) outburst. The X-ray emission is of nonthermal origin, with the spectrum well described by a power-law model with a photon index (Γ) maintaining at ~ 2. A relatively high electron temperature ($T_e > 30$ keV) is inferred from the joint fit of EP/FXT+NuSTAR spectra using the nthcomp model. No thermonuclear bursts or significant coherent pulsations are

detected in X-ray data, while a long-lasting mHz QPO signal with a centroid frequency of ~ 0.04 Hz is significantly detected by various X-ray instruments. A radio source displaying an inverted spectrum ($\alpha = 0.45 \pm 0.14$) and a potential, transient NIR counterpart are detected at the X-ray position.

Based on the source position, X-ray spectral and timing properties (stable evolution of Γ, high electron temperature, and the detection of mHz QPOs), the radio spectral shape, and the multiwavelength properties (the L_X–L_{Radio} and L_X–L_{NIR} correlations and the quasi-quiescent NIR brightness), we conclude that EP J182730.0−095633 is very likely to be a new BH LMXB captured during a faint outburst without state transitions. The discovery of EP J182730.0−095633 showcases EP's potential to find transient BHs exhibiting faint X-ray outbursts, which represent a potentially large population yet are mostly elusive to the other X-ray wide-field monitoring instruments. More of such systems are expected to be discovered in the EP era, which may advance our understandings of the underlying physical mechanism of faint-level outbursts and hopefully shed light on the "missing" puzzle of BHs in our Galaxy.

Appendix A
Multiwave Band Data Reduction

A.1. X-Rays

A.1.1. Einstein Probe

EP J182730.0–095633 was first detected in an observation starting on 2024 September 4 at 10:12:56 UT and lasting approximately 8.8 ks, on the CMOS detector No. 39 of WXT (ObsID: 06800000067). Previous individual observations covering 3 days before the detection, as well as the stacked data, did not reveal any notable source signals. The WXT

images from September 3 to 4 (first detection) are shown in panels (a)–(b) of Figure 1. It is worth noting that for the observation on September 4 the emission of the source is rather stable without short-term flaring activity. Following the discovery, an extensive monitoring campaign was conducted by EP/FXT from September 6 to 24, with a cadence of twice per day during the first week and approximately once per day thereafter. A total of 22 FXT observations were conducted and utilized for analysis. We note that the source was too faint for detection on September 23 (ObsID: 06800000118), due mainly to a significantly shorter exposure time of approximately $\sim$1000 s. The FXT was operated with module A (FXTA) in Timing Mode (TM) and module B (FXTB) in PW mode, except during the first observation, where both FXTA and FXTB were in full-frame (FF) mode. The first FXT observation provides a more precise localization of the source, with coordinates of R.A. (J2000.0) = $18^{h}27^{m}30\overset{s}{.}0$ and decl. (J2000.0) = $-9°56'33''$ (with an uncertainty of $10''$ at the 90% confidence level).

For EP/WXT, we take observations from September 1 to 6 for data analysis. Data reduction was performed using `wxtpipeline`, the standard pipeline of the WXT Data Analysis Software (WXTDAS; Y. Liu et al. 2025, in preparation), and the calibration database (CALDB) developed by the EP Science Center (EPSC). The CALDB is built based on the results of the on-ground calibration experiments (H. Cheng et al. 2025), with the procedure successfully implemented on a prototype of the WXT instrument (H. Cheng et al. 2024a). `wxtpipeline` performs calibrations to the original event data, including the coordinate transformation, flagging bad and hot pixels, and computing the pulse height amplitude invariant (PI) values, and then generates the clean event list by screening the events based on the default criteria (BR_EARTH$> = 25$ &ELV$> = 10$ &SAA$= = 0$ &ANG_DIST< 0.1). The sky image and exposure map are extracted from the clean event list. A point-source detection is then implemented on the sky image. Sources of high significance (greater than 5σ, calculated using the Li-Ma method; T. P. Li & Y. Q. Ma 1983) are cataloged, creating a detection list. For each identified source, several outputs are produced, including the light curve and spectra, the ancillary response file, the response matrix, and the background light curve and spectra. The light curves and spectra are extracted using a circular region centered on the source, with a radius of $9\overset{'}{.}1$. For the background, an annular region centered on the source is employed, with inner and outer radii of $18\overset{'}{.}2$ and $36\overset{'}{.}4$, respectively. The `wxtmerge` tool is utilized to stack multiple WXT observations.

Data reduction for FXT was performed using `fxtchain`, the standard data analysis pipeline within the FXT Data Analysis Software (FXTDAS,v1.10; H.-S. Zhao et al. 2025) developed by EPSC. This tool contains several procedures, including particle event identification, pulse-invariant value calculation, bad and hot pixel flagging, and the selection of GTIs using housekeeping data. The source was bright in the first observation carried out in FF mode, leading to a nonnegligible pileup effect. To mitigate this effect, the source photons were extracted using an annulus region centered on the target with an inner radius of $15''$ and outer radius of $80''$. The background photons were taken from a nearby source-free circular region with a radius of $150''$. For the PW imaging mode, the radii of the source and background circular regions

were both set to $60''$. For the TM mode, the source and background photons were extracted using two rectangular regions centered on the source and away from the source, respectively, both with a size of $3' \times 1'$. The solar system barycentric correction for photon arrival times was applied using the `fxtbary` tool. The TM data were excluded from the spectral analysis because of a lower spectral quality compared to those taken in the imaging mode.

A.1.2. NICER

Following the discovery of the source, NICER made several observations beginning on September 7 (PI: Huaqing Cheng). However, from September 23 onward (ObsID 7204340113), the source's flux fell below $10^{-12}\,\mathrm{erg\,s^{-1}\,cm^{-2}}$, resulting in the NICER/XTI spectra with a considerable background noise. Consequently, these observations were excluded from the data analysis. For the observations before September 23, clean event files were produced using `nicerl2` with specific settings: `underonly_range = "0-200"` and `overonly_range = "0-2"`. Focal plane modules (FPMs) 14 and 34 were not included in the analysis, as they often show elevated detector noise. Light curves and spectra were extracted using `nicerl3-lc` and `nicerl3-spec`, respectively, employing the SCORPEON background model.[42] This rigorous selection process resulted in only four observations (ObsIDs: 7204880101, 7204880102, 7204880103, and 7204880105) with clean events. Photon arrival times were corrected to the solar system barycenter using the `barycorr` tool.

A.1.3. Swift

We conducted two target-of-opportunity (ToO) observations using Swift/XRT in the Photon Counting (PC) mode, one on 2024 September 8 and another on 2024 November 1 (PI: Huaqing Cheng). The source was significantly detected in the first Swift observation, while no signals were found in the second epoch. The XRT data were processed using `xrtpipeline`, and the spectra were extracted from the level-2 cleaned data products using `xselect`. The source photons were initially extracted from a circular region centered on the target with a radius of $47''$, while the background photons were extracted from a nearby source-free circular region with a radius of $188''$. However, the pileup effect is found to be nonnegligible as indicated by the high count rate of $\sim$1.5 counts s^{-1}. To mitigate the pileup effects, photons within an inner radius of $8''$ were excluded. For the extracted X-ray spectra, we employed `xrtmkarf` to build the ancillary response files. The response matrix functions were then determined using the `quzcif` tool.

The first Swift/XRT observation provides a source position, which is enhanced by applying correction of the Swift/UVOT photometry (P. A. Evans et al. 2009): R.A. (J2000.0) = $18^{h}27^{m}30\overset{s}{.}1$ and decl. (J2000.0) = $-9°56'41''\!.4$ (uncertainty of $2''\!.1$ at the 90% confidence level). The XRT position is consistent with the FXT position with a separation of $8''$ (note that the uncertainty of FXT position is $10''$). We adopt the XRT coordinates as the X-ray position of EP J182730.0–095633.

---

[42] https://heasarc.gsfc.nasa.gov/docs/nicer/analysis_threads/scorpeon-overview/

A.1.4. NuSTAR

NuSTAR carried out an observation on 2024 September 11, with a total exposure time of approximately 20.7 ks (PI: Alessio Marino). The data were processed using the standard tools in the `NuSTARDAS` package. The cleaned level-2 event products were extracted using the `nupipeline` routine. The source photons were extracted using a circular region with a radius of 60″ centered on the source, while the background events were extracted from an annulus region with an inner radius of 90″ and an outer radius of 120″. Finally, we used `nuproducts` to extract spectra and light curves for further analysis, and we corrected the photon arrival times to the solar system barycenter using the `barycorr` tool.

A.2. Searches for Periodic X-Ray Signals

We searched for significant peaks in the power spectra extracted from the NICER and NuSTAR data sets over the whole energy range using the algorithm described by G. L. Israel & L. Stella (1996). This algorithm is based on a fast Fourier transform and accounts for non-Poissonian noise components in the Leahy-normalized (D. A. Leahy et al. 1983) power spectra. Our analysis did not reveal any significant peaks in any observations above a 3.5σ confidence threshold, calculated by considering the number of frequency trials examined. Focusing on the NICER data sets, the most stringent 3σ upper limit on the flux pulsed fraction (which we define as the semiamplitude of a sinusoidal modulation divided by the mean source count rate) was obtained from the second observation, the one with the longest exposure. This upper limit ranges between 6% and 10% for frequencies spanning 30–1000 Hz. For the NuSTAR data, after combining data sets from both FPMs, the upper limit is between 8% and 13% within the same frequency range.

We also searched for periodic signals in the second NICER observation and the NuSTAR observation using Fourier domain acceleration search techniques. Specifically, we employed the `accelsearch` pipeline from the `PRESTO`[43] pulsar timing software package (S. M. Ransom et al. 2002) to search for signals within the frequency range of 1–1000 Hz, summing up to eight harmonics. To account for potential power drifts in the Fourier domain, we allowed the powers of signals to drift by up to 200 frequency bins. Moreover, we conducted a "jerk" search, allowing the powers of the signals to drift by up to 600 frequency derivative bins, as described by B. C. Andersen & S. M. Ransom (2018). No promising signals were detected.

For EP/FXT observations, we also searched the pulsed signal using powspec and further checked the signal around the QPO frequency with the blind search technique developed by the Fermi-LAT collaboration (W. B. Atwood et al. 2006). No confirmed signals were detected, consistent with the result obtained from NICER and NuSTAR data. In the end, the upper limit for the FXT timing mode observation is between 6% and 13% for frequencies spanning 30–1000 Hz using the algorithm described by G. L. Israel & L. Stella (1996).

---

43 https://github.com/scottransom/presto

A.3. Optical and Infrared

A.3.1. GROND

EP J182730.0–095633 was observed with GROND (J. Greiner et al. 2008), mounted at the MPG 2.2 m telescope at ESO's La Silla observatory for six nights from 2024 September 7 to October 1 (see Table B2). Observations were performed simultaneously in the g', r', i', J, H, and K_s bands with typical exposures of 30 minutes per band and observation. The data were reduced using the standard IRAF-based GROND pipeline (T. Krühler et al. 2008). The photometry was calibrated against Pan-STARRS DR1 (K. C. Chambers et al. 2016) (g', r', i') and the Two Micron All Sky Survey (2MASS) catalog (M. F. Skrutskie et al. 2006; J, H, and K_s) and converted into the AB system.

A.3.2. SVOM/VT

The VT is an optical telescope on board the SVOM mission (J. Wei et al. 2016). The effective aperture is 43 cm. The FOV is $26' \times 26'$, giving the pixel scale of 0.″76. It conducts the observation with two broadband channels VT_B and VT_R simultaneously, covering 400–650 nm and 650–1000 nm, respectively. Detailed information on VT can be referred to Y. L. Qiu et al. (2025, in preparation). EP J182730.0–095633 was observed twice by VT during its commissioning phase via ToO mode, one on 13:23:58 UT, 2024 September 6 and the other on 21:45:55 UT, 2024 September 28. The exposure time was set to be 20 s for single frame. All the data were processed in a standard manner, including zero correction, dark correction, and flat-field correction. After preprocessing, the images for each band obtained during each observation were stacked to increase the signal-to-noise ratio.

A.3.3. NOT

The optical photometry follow-up observation was carried out using the 2.56 m NOT (Roque de los Muchachos observatory, La Palma, Spain) equipped with the Alhambra Faint Object Spectrograph and Camera at 20:42:54 UT on 2024 September 7, i.e., 3.4 days after the trigger, and 4×180 s frames were obtained in the Sloan Digital Sky Survey r band. The NOT data are reduced by standard procedures with the IMAGE REDUCTION AND ANALYSIS FACILITY (IRAF) v2.16 (D. Tody 1986), including bias subtraction, flat-field correction, and image combination.

A.3.4. TRT

We began to observe EP J182730.0–095633 using the 0.7 m telescope of the TRT network, located at Sierra Remote Observatories, USA. The observation started at 02:34:30 UT on 2024 September 8, i.e., 3.7 days after the trigger and several frames were obtained in the Johnson B band. Raw data were processed automatically using the TRT's standard data reduction pipeline. We stack clean science frames using IRAF to improve the signal-to-noise ratio.

A.3.5. ALT100C

ALT100C is a 1 m telescope located at Altay Observatory, Xinjiang, China. The observation of EP J182730.0–095633 was conducted at 14:49:20 UT on 2024 September 8, i.e., 4.2

days after the trigger in the g, r, and i bands. The data are also reduced by IRAF and calibrated with nearby Pan-STARRS stars.

A.3.6. TNT

TNT (F. Huang et al. 2012), an 80 cm Cassegrain reflecting telescope located at Xinglong Observatory of the National Astronomical Observatories of China (NAOC), was used to observe the field of the X-ray transient EP J182730.0–095633. Observations were conducted in the r and i bands, obtaining 6×600 s exposures per band, with a median observation date of 2024-10-11T11:33:50. After the bias and flat-field correction, the images were stacked by the imcombine program in IRAF. The photometric measurements were carried out using SEXTRACTOR (E. Bertin & S. Arnouts 1996). The automatic aperture photometry was derived from Kron's "first moment" algorithm (R. G. Kron 1980). The instrumental magnitude was then calibrated to Pan-STARR DR1.

A.3.7. Mephisto

Mephisto[44] is a wide-field ground-based telescope with a 1.6 m primary mirror featuring an FOV of 2 deg^2 (X. Yuan et al. 2020). Observations were conducted at 16:11:28 UT on 2024 September 7, i.e., 3.2 days after the trigger, in the v, r, and z bands. For data reduction, the raw frames were processed through a dedicated preprocessing pipeline developed for Mephisto. This pipeline includes bias subtraction, dark subtraction, flat-fielding, and cosmic-ray removal. Photometric calibration was performed using the Gaia Blue Photometer (BP)/Red Photometer (RP) low-resolution spectra (BP/RP Spectrophotometry (XP) spectra) of nonvariable stars. Since there were no detections in either the single frames or the stacked frames for each band, we calculated the 5σ limiting magnitudes for each frame based on the image's full width at half-maximum and the background fluctuations at the target's position.

A.4. Radio

A.4.1. ATCA

Two radio observations were carried out using ATCA at 4 cm, one on 2024 September 12 from 09:00 to 14:00 UT (A. Wang et al. 2024a), and the other on 2024 September 21 from 07:30 to 12:30 UT. The ATCA observations were conducted as part of project C3615 (PI: Yanan Wang). The central frequencies were set at 5.5 and 9 GHz, each with a bandwidth of 2 GHz. These observations were coordinated with EP/FXT observations to investigate any correlations between the radio and X-ray emissions. Data were processed using the Common Astronomy Software Applications (CASA; J. P. McMullin et al. 2007; CASA Team et al. 2022) with standard interferometric imaging methods. Flux density and gain calibrators 1934–638 and 1829–106 were used for the calibration.

A.4.2. MeerKAT

We observed the position of EP J182730.0–095633 with the MeerKAT radio telescope (F. Camilo et al. 2018; J. Jonas 2018), as part of program SCI-20230907-JB-01 (PIs Bright and Carotenuto). We conducted three observations, each with the same total on-source time of 42 minutes. We observed quasi-simultaneously at L band and S band, the first at a central frequency of 1.28 GHz with a total bandwidth of 856 MHz and the second at 3.06 GHz (S band, S4) with a total bandwidth of 875 MHz. The first observation started on 2024 September 21 at 15:16 UTC (L band) and 16:51 UTC (S band). The second observation was performed on 2024 October 21 at 13:45 UTC (S band) and on 2024 October 22 at 19:09 UTC (L band), while the third observation was conducted on 2025 October 28 at 16:44 UTC (S band) and 18:14 UTC (L band). PKS J1939–6342 and PKS 1830–211 were used as flux and complex gain calibrators, respectively. The data were reduced with the OxKAT pipeline (I. Heywood 2020), which performs standard flagging, calibration, and imaging using tricolour (B. V. Hugo et al. 2022), CASA, and WSCLEAN (A. R. Offringa et al. 2014), respectively. In the imaging step, we adopted a Briggs weighting scheme with a -0.3 robust parameter. The typical values for the image rms noise are $\sim$10 μJy beam^{-1} at S band and 20–30 μJy beam^{-1} at L band, due to the presence of diffuse emission in the field, stronger at lower frequencies.

Appendix B
Supplementary Material

In this Appendix, we present the detailed results of the X-ray spectral fitting (Table B1), optical and infrared follow-up observations (Table B2), and radio follow-up observations (Table B3). The evolutionary trend of the photon index Γ using two different data analysis strategies is presented in Figure B1, and thePSDs of EP/FXT and NICER during the X-ray outburst are presented in Figure B2. The rms spectrum and relation between the low frequency break (ν_{bb}) of the PSD and the centroid frequency of the QPO signal (ν_{qpo}) are presented in Figure B3.
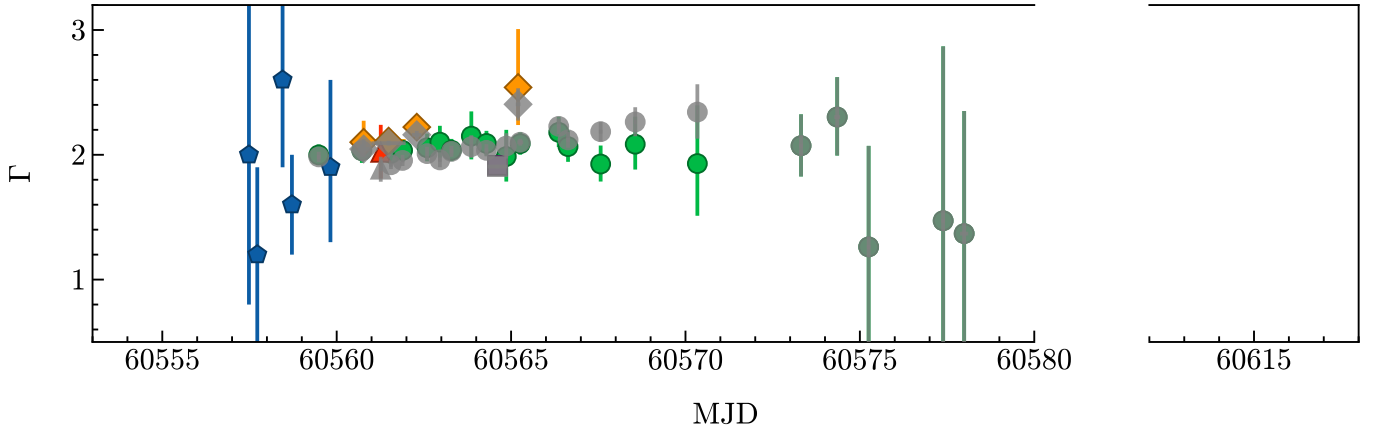

Figure B1. Evolutionary trend of the photon index Γ using two different data analysis strategies for EP/FXT, NICER, Swift/XRT, and NuSTAR data. The results shown as gray symbols are obtained by fixing the column density N_H to the typical parameter value of 3.1×10^{22} cm^{-2} during the outburst. The result obtained with variable column density (same as in Figure 3) is also plotted for comparison.

Table B1
X-ray Spectral Fitting Results of EP J182730.0–095633

Obs. Date	$T - T_0$ (days)	Instrument	ObsID	N_H (10^{22} cm^{-2})	Γ	$F_{\mathrm{unabsorbed},0.5-10}$ ($\times 10^{-11}$ erg s^{-1} cm^{-2})	χ^2/dof	Exposure (s)
2024-09-01/02/03	−1.8	EP/WXT	06800000061/63/68	3.1*	2.0*	< 4.3	⋯	27230
2024-09-04	0	EP/WXT	06800000067	3.1*	$2.0^{+1.3}_{-1.2}$	14^{+10}_{-5}	58.3/68	6075
⋯	0.3	EP/WXT	08500000148	3.1*	$1.2^{+0.7}_{-0.7}$	37^{+16}_{-9}	99.8/104	9246
2024-09-05	1.0	EP/WXT	06800000071	3.1*	$2.6^{+0.7}_{-0.7}$	52^{+29}_{-15}	50.1/47	2987
⋯	1.3	EP/WXT	06800000069	3.1*	$1.6^{+0.4}_{-0.4}$	40^{+7}_{-6}	130.5/146	9155
2024-09-06	2.1	EP/FXT	06800000074	$3.1^{+0.1}_{-0.1}$	$2.00^{+0.08}_{-0.08}$	35^{+2}_{-2}	307.8/297	5966
⋯	2.4	EP/WXT	06800000070	3.1*	$1.9^{+0.7}_{-0.6}$	30^{+8}_{-7}	129.5/94	6070
2024-09-07	3.3	EP/FXT	06800000081	$3.3^{+0.2}_{-0.2}$	$2.03^{+0.10}_{-0.10}$	23^{+2}_{-1}	195.6/189	2983
⋯	3.3	NICER/XTI	7204880101	$3.2^{+0.2}_{-0.2}$	$2.1^{+0.14}_{-0.17}$	27^{+3}_{-2}	109.39/117	223
2024-09-08	3.8	Swift/XRT	00016796001	$3.4^{+0.5}_{-0.5}$	$2.02^{+0.22}_{-0.21}$	20^{+4}_{-3}	61.5/50	2864
⋯	4.1	NICER/XTI	7204880102	$3.1^{+0.1}_{-0.1}$	$2.11^{+0.06}_{-0.04}$	$25.3^{+0.7}_{-0.6}$	607.69/603	3921
⋯	4.1	EP/FXT	06800000079	$3.3^{+0.1}_{-0.1}$	$2.01^{+0.07}_{-0.07}$	$21.0^{+1.0}_{-0.9}$	303.7/276	5941
⋯	4.5	EP/FXT	06800000080	$3.3^{+0.2}_{-0.1}$	$2.04^{+0.09}_{-0.09}$	20^{+1}_{-1}	221.8/209	3935
2024-09-09	5.2	EP/FXT	06800000082	$3.2^{+0.2}_{-0.2}$	$2.06^{+0.11}_{-0.11}$	18^{+1}_{-1}	145.3/151	2984
⋯	5.5	EP/FXT	06800000083	$3.4^{+0.2}_{-0.2}$	$2.10^{+0.13}_{-0.13}$	17^{+2}_{-1}	154.8/128	2716
⋯	4.9	NICER/XTI	7204880103	$3.2^{+0.1}_{-0.1}$	$2.22^{+0.08}_{-0.08}$	24^{+1}_{-1}	527.82/515	1543
2024-09-10	5.9	EP/FXT	06800000087	$3.1^{+0.2}_{-0.2}$	$2.04^{+0.09}_{-0.09}$	$14.9^{+0.9}_{-0.8}$	231.7/218	5319
⋯	6.4	EP/FXT	06800000088	$3.3^{+0.3}_{-0.3}$	$2.15^{+0.20}_{-0.19}$	14^{+2}_{-2}	75.5/64	1580
2024-09-11	6.9	EP/FXT	06800000089	$3.2^{+0.2}_{-0.2}$	$2.09^{+0.10}_{-0.10}$	$12.8^{+0.9}_{-0.7}$	188.4/185	5361
⋯	7.2	NuSTAR	91001334002	3.7 ± 1.3	1.92 ± 0.03	8.2 ± 0.3	718.7/765	2690
⋯	7.4	EP/FXT	06800000090	$2.9^{+0.4}_{-0.3}$	$2.00^{+0.21}_{-0.20}$	11^{+2}_{-1}	82.5/57	1500
2024-09-12	7.8	NICER/XTI	7204880105	$3.3^{+0.6}_{-0.4}$	$2.54^{+0.47}_{-0.30}$	15^{+6}_{-3}	168.8/165	703
⋯	7.8	EP/FXT	06800000091	$3.1^{+0.2}_{-0.1}$	$2.09^{+0.09}_{-0.09}$	$10.7^{+0.7}_{-0.6}$	240.7/221	7581
2024-09-13	8.9	EP/FXT	06800000095	$3.0^{+0.2}_{-0.2}$	$2.18^{+0.12}_{-0.12}$	$7.6^{+0.7}_{-0.6}$	132.5/133	5886
⋯	9.2	EP/FXT	06800000096	$3.0^{+0.2}_{-0.2}$	$2.07^{+0.13}_{-0.12}$	$6.8^{+0.6}_{-0.5}$	144.3/124	5976
2024-09-14	10.1	EP/FXT	06800000097	$2.6^{+0.2}_{-0.2}$	$1.93^{+0.15}_{-0.14}$	$4.5^{+0.4}_{-0.3}$	118.1/97	5978
2024-09-15	11.1	EP/FXT	06800000098	$2.8^{+0.3}_{-0.3}$	$2.08^{+0.22}_{-0.20}$	$3.3^{+0.5}_{-0.3}$	39.9/48	4091
2024-09-17	12.9	EP/FXT	06800000110	$2.4^{+0.7}_{-0.6}$	$1.93^{+0.47}_{-0.42}$	$1.5^{+0.5}_{-0.2}$	19.4/16	2992
2024-09-20	15.9	EP/FXT	06800000111	3.1*	$2.07^{+0.25}_{-0.25}$	$0.49^{+0.06}_{-0.05}$	132.7/114	5987
2024-09-21	16.9	EP/FXT	06800000114	3.1*	$2.30^{+0.32}_{-0.31}$	$0.24^{+0.04}_{-0.03}$	100.1/85	8979
2024-09-22	17.8	EP/FXT	06800000117	3.1*	$1.26^{+0.81}_{-0.81}$	$0.059^{+0.003}_{-0.002}$	11.4/17	5960
2024-09-23	19.4	EP/FXT	06800000118	3.1*	2.0*	< 0.068	⋯	1387
2024-09-24	20.0	EP/FXT	06800000120	3.1*	$1.47^{+1.40}_{-1.40}$	$0.043^{+0.045}_{-0.018}$	10.8/14	5842
⋯	20.6	EP/FXT	06800000123	3.1*	$1.37^{+0.98}_{-0.98}$	$0.030^{+0.020}_{-0.012}$	13.5/12	8095
2024-11-01	57.9	Swift/XRT	00016796002	3.1*	2.0*	< 0.037	...	2582

Note. T_0 is set as the starting time of the WXT observation during which the source was first detected, at 2024-09-04T10:12:56 (UTC). The parameters marked with an asterisk were held fixed at the quoted values in the fits.

14

Table B2
Optical and Infrared Follow-up Observations of EP J182730.0–095633

Obs. Date	$T - T_0$ (days)	Instrument	Filter	Detection	Observed Magnitude or 5σ Upper Limit
2024-09-06	2.1	SVOM/VT	VT_R, VT_B	N	>21.4 / > 22.9
2024-09-07	2.6	GROND	J, H, K_s	Y	17.97 ± 0.22^J / 16.73 ± 0.13^H / 16.32 ± 0.13^K
⋯	⋯	⋯	g', r', i'	N	$>23^g$ / $>22.6^r$ / $>21.5^i$
⋯	3.2	Mephisto	v, r, z	N	$>20.7^v$ / $>20.5^r$ / $>19.36^z$
⋯	3.4	NOT	r	Y	23.87 ± 0.35^r
2024-09-08	3.6	GROND	J, H, K_s	Y	18.09 ± 0.18^J / 16.81 ± 0.18^H / 16.43 ± 0.16^K
⋯	⋯	⋯	g', r', i'	Y	$>23.9^g$ / 23.86 ± 0.30^r / 21.77 ± 0.10^i
⋯	3.7	TRT	B	N	$>21.4^B$
⋯	4.2	ALT100C	r, g, i	N	$>22.3^r$ / $>21.7^g$ / $>20.9^i$
2024-09-09	4.6	GROND	J, H, K_s	Y	18.01 ± 0.18^J / 16.93 ± 0.16^H / 16.50 ± 0.15^K
⋯	⋯	⋯	g', r', i'	Y	$>23.6^g$ / $>23.2^r$ / 21.95 ± 0.15^i
2024-09-11	6.7	GROND	J, H, K_s	N	-/-/ -
⋯	⋯	⋯	g', r', i'	N	$>21.2^g$ / $>21.5^r$ / $>20.7^i$
2024-09-18	13.7	GROND	J, H, K_s	N	$>19.2^g$ / $>17.7^r$ / $>17.4^i$
⋯	⋯	⋯	g', r', i'	N	$>21.7^g$ / $>22.3^r$ / $>21.6^i$
2024-09-28	24.5	SVOM/VT	VT_R, VT_B	N	> 21.6 / > 22.3
2024-10-01	27.6	GROND	J, H, K_s	N	-/-/ -
⋯	⋯	⋯	g', r', i'	N	$>21.0^g$ / $>21.2^r$ / $>21.0^i$
2024-10-11	37.0	TNT	r, i	N	$>18.24^r$ / $>17.54^i$

Note. T_0 is set as the starting time of the WXT observation during which the source was first detected, at 2024-09-04T10:12:56 (UTC). With poor seeing conditions during the GROND observations in the J, H, and K bands on September 11 and October 1, it was not feasible to accurately constrain the flux of the source, due to its proximity to other brighter sources. As a result, the magnitudes in these bands are not provided.

Table B3
Radio Follow-up Observations of EP J182730.0–095633

Obs. Date	$T - T_0$ (days)	Instrument	Filter	Detection	Peak Flux Density/3σ Upper Limit (μJy beam^{-1})
2024-09-12	7.9	ATCA	5.5 GHz	Y	101.2 ± 5.4
⋯	7.9	ATCA	9 GHz	Y	126.3 ± 5.2
2024-09-21	16.9	ATCA	5.5 GHz	N	<57
⋯	16.9	ATCA	9 GHz	N	<60
⋯	17.2	MeerKAT	1.28 GHz (L band)	N	<69
⋯	17.3	MeerKAT	3.06 GHz (S band)	Y	33 ± 4
2024-10-21	47.1	MeerKAT	3.06 GHz (S band)	N	<36
2024-10-21	48.4	MeerKAT	1.28 GHz (L band)	Y	58 ± 12
2024-10-22	54.3	MeerKAT	3.06 GHz (S band)	N	<36
2024-10-22	54.3	MeerKAT	1.28 GHz (L band)	N	<105

Note. T_0 is set as the starting time of the WXT observation during which the source was first detected, at 2024-09-04T10:12:56 (UTC).
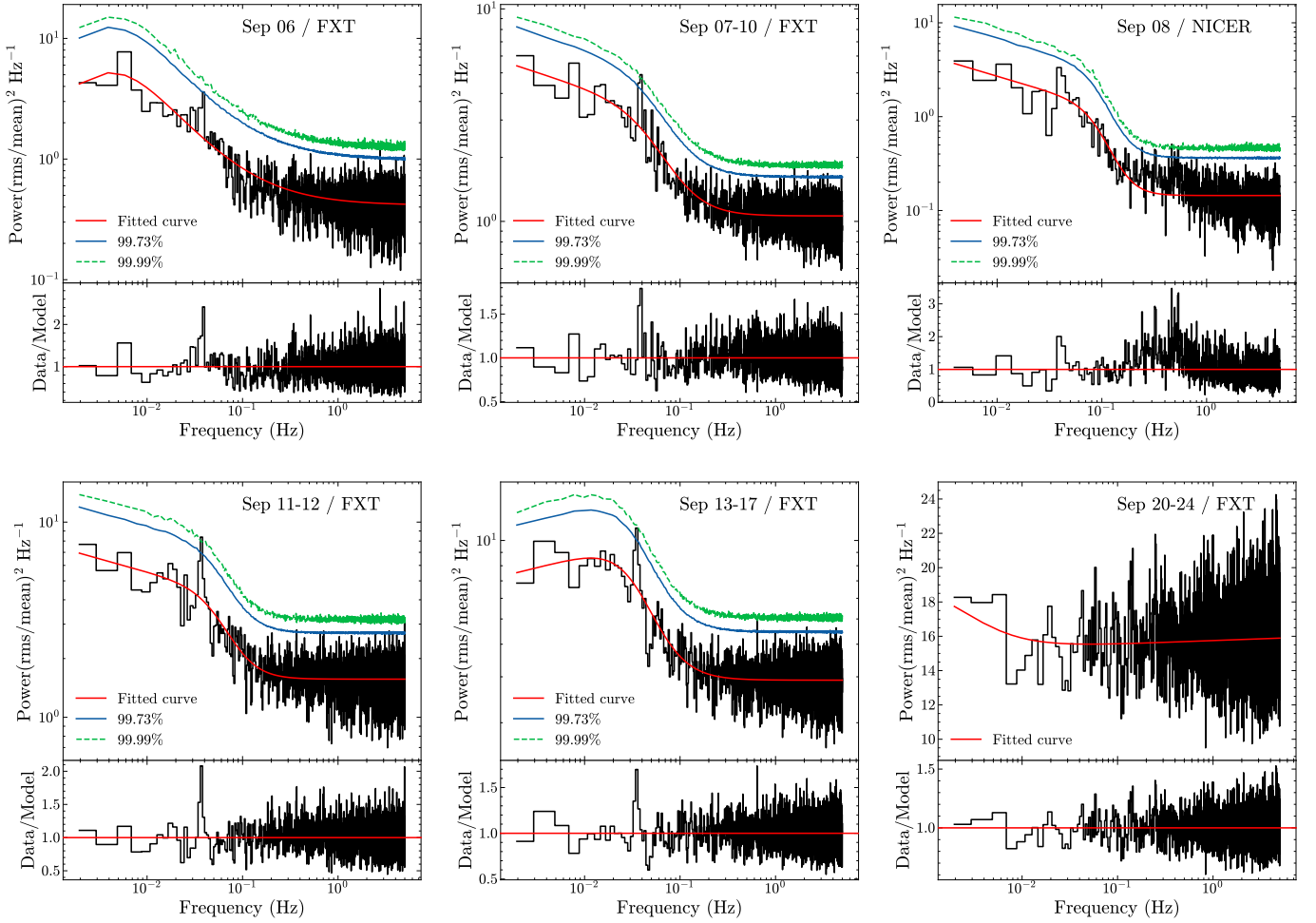
Figure B2. PSDs of EP/FXT and NICER during the outburst. The centroid frequency of the most prominent QPO holds steady at ~0.04 Hz. For the EP/FXTA (TM mode) data, we combined them to improve the signal-to-noise ratio. The absence of the QPO signal in the final FXT data set (from September 20 to 24) is likely attributed to the extremely low count rate of the source during this period.
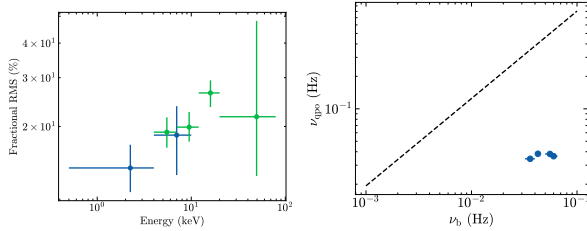

Figure B3. Left panel: the rms spectrum calculated using the same data set as Figure 2 (EP/FXT+NuSTAR on 2024 September 11). The blue circles are from EP-FXT, and green circles are from NuSTAR. Right panel: the relation between the low-frequency break (ν_b) of the PSD and the centroid frequency of the QPO signal (ν_{qpo}), with the results of EP J182730.0–095633 denoted as blue circles. Here we use the PSDs from September 7–10 (FXT), September 11 (NuSTAR), September 11–12 (FXT), and September 13–17 (FXT), where the QPO significance exceeds 3σ. The black dashed line is the empirical W–K relation between the two variables for type C LFQPOs. ν_{qpo} are 38.2 ± 0.2 mHz, 38.3 ± 0.3 mHz, 36.4 ± 0.4 mHz, and 34.4 ± 0.4 mHz for the four PSDs, respectively, while ν_b are 55 ± 6 mHz, 43 ± 2 mHz, 60 ± 5 mHz, and 36 ± 4 mHz.

ORCID iDs

H. Q. Cheng ⓘ https://orcid.org/0000-0003-4200-9954
Q. C. Zhao ⓘ https://orcid.org/0000-0001-9893-8248
L. Tao ⓘ https://orcid.org/0000-0002-2705-4338
H. Feng ⓘ https://orcid.org/0000-0001-7584-6236

F. Coti Zelati ⓘ https://orcid.org/0000-0001-7611-1581
A. L. Wang ⓘ https://orcid.org/0000-0002-7351-5801
M. Y. Ge ⓘ https://orcid.org/0000-0002-2749-6638
A. Rau ⓘ https://orcid.org/0000-0001-5990-6243
A. Marino ⓘ https://orcid.org/0000-0001-5674-4664
L. Zhang ⓘ https://orcid.org/0000-0003-4498-9925
W. J. Zhang ⓘ https://orcid.org/0009-0003-9214-7316
F. Carotenuto ⓘ https://orcid.org/0000-0002-0426-3276
L. Ji ⓘ https://orcid.org/0000-0001-9599-7285
C. C. Jin ⓘ https://orcid.org/0000-0002-2006-1615
D. Y. Li ⓘ https://orcid.org/0000-0002-4562-7179
B. F. Liu ⓘ https://orcid.org/0000-0001-9920-4019
E. L. Qiao ⓘ https://orcid.org/0000-0001-8319-6034
N. Rea ⓘ https://orcid.org/0000-0003-2177-6388
R. Soria ⓘ https://orcid.org/0000-0002-4622-796X
S. Wang ⓘ https://orcid.org/0000-0003-3116-5038
Z. Yan ⓘ https://orcid.org/0000-0002-5385-9586
B. Zhang ⓘ https://orcid.org/0000-0002-9725-2524
G. B. Zhang ⓘ https://orcid.org/0000-0001-8630-5435
S. N. Zhang ⓘ https://orcid.org/0000-0001-5586-1017
A. Beardmore ⓘ https://orcid.org/0000-0001-5186-5950
J. S. Bright ⓘ https://orcid.org/0000-0002-7735-5796
X. L. Chen ⓘ https://orcid.org/0009-0000-4068-1320
S. Y. Fu ⓘ https://orcid.org/0009-0002-7730-3985
J. P. U. Fynbo ⓘ https://orcid.org/0000-0002-8149-8298

J. W. Hu https://orcid.org/0000-0002-0779-1947
J. J. Jin https://orcid.org/0000-0002-8402-3722
P. G. Jonker https://orcid.org/0000-0001-5679-0695
A. K. H. Kong https://orcid.org/0000-0002-5105-344X
E. Kuulkers https://orcid.org/0000-0002-5790-7290
C. K. Li https://orcid.org/0000-0001-5798-4491
H. L. Li https://orcid.org/0000-0002-7457-4192
C. X. Liu https://orcid.org/0000-0001-5561-2010
H.-Y. Liu https://orcid.org/0000-0002-2412-5751
J. Z. Liu https://orcid.org/0000-0002-7420-6744
X. W. Liu https://orcid.org/0000-0003-1295-2909
Z. Lu https://orcid.org/0009-0001-8477-9466
C.-Y. Ng https://orcid.org/0000-0002-5847-2612
S. Tinyanont https://orcid.org/0000-0002-1481-4676
Y. Wang https://orcid.org/0000-0002-8385-7848
Jianfeng Wu https://orcid.org/0000-0001-7349-4695
D. Xu https://orcid.org/0000-0003-3257-9435
Y. K. Yan https://orcid.org/0009-0003-7431-650X
Y.-P. Yang https://orcid.org/0000-0001-6374-8313
Y. Chen https://orcid.org/0000-0001-9834-2196
S. M. Jia https://orcid.org/0000-0002-5203-8321
Y. F. Xu https://orcid.org/0000-0002-7397-811X

References

Alabarta, K., Altamirano, D., Méndez, M., et al. 2021, MNRAS, 507, 5507
Altamirano, D., & Strohmayer, T. 2012, ApJL, 754, L23
Andersen, B. C., & Ransom, S. M. 2018, ApJL, 863, L13
Armas Padilla, M., Wijnands, R., Altamirano, D., et al. 2014, MNRAS, 439, 3908
Arnaud, K. A. 1996, in ASP Conf. Ser. 101, Astronomical Data Analysis Software and Systems V, ed. G. H. Jacoby & J. Barnes (San Francisco, CA: ASP), 17
Atapin, K., Fabrika, S., & Caballero-García, M. D. 2019, MNRAS, 486, 2766
Atwood, W. B., Ziegler, M., Johnson, R. P., & Baughman, B. M. 2006, ApJL, 652, L49
Avakyan, A., Neumann, M., Zainab, A., et al. 2023, A&A, 675, A199
Bahramian, A., & Degenaar, N. 2023, in Handbook of X-ray and Gamma-ray Astrophysics, ed. B. Cosimo & A. Santangelo, 120 (Singapore: Springer Nature)
Bahramian, A., & Rushton, A. 2022, bersavosh/XRB-LrLx_pub: update 20220908, v220908, Zenodo, doi:10.5281/zenodo.7059313
Banerjee, S., Gilfanov, M., Bhattacharyya, S., & Sunyaev, R. 2020, MNRAS, 498, 5353
Barthelmy, S. D., Barbier, L. M., Cummings, J. R., et al. 2005, SSRv, 120, 143
Belloni, T. 2010, The Jet Paradigm, 794 (Berlin: Springer)
Belloni, T., & Hasinger, G. 1990, A&A, 230, 103
Belloni, T., Motta, S. E., & Muñoz-Darias, T. 2011, BASI, 39, 409
Benz, A. O., & Güdel, M. 2010, ARA&A, 48, 241
Beri, A., Gaur, V., Charles, P., et al. 2023, MNRAS, 522, 4598
Bertin, E., & Arnouts, S. 1996, A&AS, 117, 393
Bloom, J. S., Giannios, D., Metzger, B. D., et al. 2011, Sci, 333, 203
Bozzo, E., Ferrigno, C., Stevens, J., et al. 2011, A&A, 535, L1
Bozzo, E., Papitto, A., Ferrigno, C., & Belloni, T. M. 2014, A&A, 570, L2
Brandt, S., Lund, N., & Rao, A. R. 1990, AdSpR, 10, 239
Brown, G. E., & Bethe, H. A. 1994, ApJ, 423, 659
Buisson, D. J. K., Fabian, A. C., Barret, D., et al. 2019, MNRAS, 490, 1350
Burke, M. J., Gilfanov, M., & Sunyaev, R. 2017, MNRAS, 466, 194
Burrows, D. N., Kennea, J. A., Ghisellini, G., et al. 2011, Natur, 476, 421
Camilo, F., Scholz, P., Serylak, M., et al. 2018, ApJ, 856, 180
Cardelli, J. A., Clayton, G. C., & Mathis, J. S. 1989, ApJ, 345, 245
CASA Team, Bean, B., Bhatnagar, S., et al. 2022, PASP, 134, 114501
Casella, P., Belloni, T., Homan, J., & Stella, L. 2004, A&A, 426, 587
Cash, W. 1979, ApJ, 228, 939
Chambers, K. C., Magnier, E. A., Metcalfe, N., et al. 2016, arXiv:1612.05560
Chen, W., Shrader, C. R., & Livio, M. 1997, ApJ, 491, 312
Chen, Y., Cui, W., Han, D., et al. 2020, Proc. SPIE, 11444, 114445B
Cheng, H., Ling, Z., Zhang, C., et al. 2024a, ExA, 57, 10
Cheng, H., Zhang, C., Ling, Z., et al. 2025, arXiv:2505.18939
Cheng, H. Q., Wen, S. X., Wang, Y., et al. 2024b, ATel, 16805, 1

Corbel, S., Coriat, M., Brocksopp, C., Tzioumis, A. K., Fender, R. P., et al. 2013, MNRAS, 428, 2500
Corral-Santana, J. M., Casares, J., Muñoz-Darias, T., et al. 2013, Sci, 339, 1048
Corral-Santana, J. M., Casares, J., Muñoz-Darias, T., et al. 2016, A&A, 587, A61
Degenaar, N., & Wijnands, R. 2009, A&A, 495, 547
Del Santo, M., Nucita, A. A., Lodato, G., et al. 2014, MNRAS, 444, 93
Dewangan, G. C., Titarchuk, L., & Griffiths, R. E. 2006, ApJL, 637, L21
Díaz Trigo, M., Altamirano, D., Dinçer, T., et al. 2018, A&A, 616, A23
Drlica-Wagner, A., Bechtol, K., Mau, S., et al. 2020, ApJ, 893, 47
Dubus, G., Hameury, J. M., & Lasota, J. P. 2001, A&A, 373, 251
El Byad, H., Bachetti, M., Columbu, S., et al. 2025, ApJ, 989, 202
Evans, P. A., Beardmore, A. P., Page, K. L., et al. 2009, MNRAS, 397, 1177
Evans, P. A., Page, K. L., Osborne, J. P., et al. 2020, ApJS, 247, 54
Fu, S. Y., An, J., Jiang, S. Q., et al. 2024, ATel, 16807, 1
Gehrels, N., Chincarini, G., Giommi, P., et al. 2004, ApJ, 611, 1005
Gendreau, K. C., Arzoumanian, Z., Adkins, P. W., et al. 2016, Proc. SPIE, 9905, 99051H
Greiner, J., Bornemann, W., Clemens, C., et al. 2008, PASP, 120, 405
Grimm, H. J., Gilfanov, M., & Sunyaev, R. 2002, A&A, 391, 923
Hailey, C. J., Mori, K., Bauer, F. E., et al. 2018, Natur, 556, 70
Hands, A. D. P., Warwick, R. S., Watson, M. G., & Helfand, D. J. 2004, MNRAS, 351, 31
Harrison, F. A., Craig, W. W., Christensen, F. E., et al. 2013, ApJ, 770, 103
Heinke, C. O., Bahramian, A., Degenaar, N., & Wijnands, R. 2015, MNRAS, 447, 3034
Heywood, I., 2020 oxkat: Semi-automated Imaging of MeerKAT Observations, Astrophysics Source Code Library, ascl:2009.003
HI4PI Collaboration, Ben Bekhti, N., Flöer, L., et al. 2016, A&A, 594, A116
Huang, F., Li, J.-Z., Wang, X.-F., et al. 2012, RAA, 12, 1585
Hugo, B. V., Perkins, S., Merry, B., Mauch, T., & Smirnov, O. M. 2022, in ASP Conf. Ser. 532, ed. J. E. Ruiz, F. Pierfederici, & P. Teuben (San Francisco, CA: ASP), 541
Hunter, J. D. 2007, CSE, 9, 90
Ichimaru, S. 1977, ApJ, 214, 840
Ingram, A. R., & Motta, S. E. 2019, NewAR, 85, 101524
Israel, G. L., & Stella, L. 1996, ApJ, 468, 369
Jonas, J. 2018, Proceedings of MeerKAT Science: On the Pathway to the SKA —PoS (MeerKAT2016), 277, 001
Kalemci, E., Kara, E., & Tomsick, J. A. 2022, in Handbook of X-ray and Gamma-ray Astrophysics, ed. C. Bambi & A. Sangangelo, 9 (Singapore: Springer Nature)
King, A. R., & Ritter, H. 1998, MNRAS, 293, L42
Kron, R. G. 1980, ApJS, 43, 305
Krühler, T., Küpcü Yoldaş, A., Greiner, J., et al. 2008, ApJ, 685, 376
Kuulkers, E., Ferrigno, C., Kretschmar, P., et al. 2021, NewAR, 93, 101629
Leahy, D. A., Elsner, R. F., & Weisskopf, M. C. 1983, ApJ, 272, 256
Levan, A. J., Tanvir, N. R., Brown, G. C., et al. 2016, ApJ, 819, 51
Levine, A. M., Bradt, H., Cui, W., et al. 1996, ApJL, 469, L33
Lewin, W. H. G., van Paradijs, J., & van den Heuvel, E. P. J. 1995, X-ray Binaries, 26 (Cambridge: Cambridge Univ. Press)
Li, T. P., & Ma, Y. Q. 1983, ApJ, 272, 317
Li, Y., Yan, Z., Gao, C., & Yu, W. 2025, MNRAS, 538, 1143
Lyu, M., Zhang, G., Méndez, M., et al. 2020, ApJ, 895, 120
Mancuso, G. C., Altamirano, D., Bult, P., et al. 2023, MNRAS, 521, 5616
Mancuso, G. C., Altamirano, D., García, F., et al. 2019, MNRAS, 486, L74
Matsuoka, M., Kawasaki, K., Ueno, S., et al. 2009, PASJ, 61, 999
McMullin, J. P., Waters, B., Schiebel, D., Young, W., & Golap, K. 2007, in ASP Conf. Ser. 376, Astronomical Data Analysis Software and Systems XVI, ed. R. A. Shaw, F. Hill, & D. J. Bell (San Francisco, CA: ASP), 127
Meier, D. L. 2012, Black Hole Astrophysics: The Engine Paradigm (Berlin: Springer)
Motta, S., Muñoz-Darias, T., Casella, P., Belloni, T., & Homan, J. 2011, MNRAS, 418, 2292
Muno, M. P., Lu, J. R., Baganoff, F. K., et al. 2005a, ApJ, 633, 228
Muno, M. P., Pfahl, E., Baganoff, F. K., et al. 2005b, ApJL, 622, L113
Narayan, R., & Yi, I. 1994, ApJL, 428, L13
Narayan, R., & Yi, I. 1995a, ApJ, 444, 231
Narayan, R., & Yi, I. 1995b, ApJ, 452, 710
Nasa High Energy Astrophysics Science Archive Research Center (Heasarc), 2014 HEAsoft: Unified Release of FTOOLS and XANADU, Astrophysics Source Code Library, ascl:1408.004
Offringa, A. R., McKinley, B., Hurley-Walker, N., et al. 2014, MNRAS, 444, 606
Pasham, D. R., Cenko, S. B., Levan, A. J., et al. 2015, ApJ, 805, 68

Pecaut, M. J., & Mamajek, E. E. 2013, ApJS, 208, 9
Pecaut, M. J., Mamajek, E. E., & Bubar, E. J. 2012, ApJ, 746, 154
Plotkin, R. M., Gallo, E., & Jonker, P. G. 2013, ApJ, 773, 59
Porquet, D., Grosso, N., Burwitz, V., et al. 2005, A&A, 430, L9
Qiao, E., & Liu, B. F. 2020, MNRAS, 496, 2704
Ransom, S. M., Eikenberry, S. S., & Middleditch, J. 2002, AJ, 124, 1788
Remillard, R. A., & McClintock, J. E. 2006, ARA&A, 44, 49
Revnivtsev, M., Churazov, E., Gilfanov, M., & Sunyaev, R. 2001, A&A, 372, 138
Revnivtsev, M., Sunyaev, R., & Borozdin, K. 2000, A&A, 361, L37
Rodriguez, J., Corbel, S., Hannikainen, D. C., et al. 2004, ApJ, 615, 416
Russell, D. M., Fender, R. P., Hynes, R. I., et al. 2006, MNRAS, 371, 1334
Sakano, M., Warwick, R. S., Decourchelle, A., & Wang, Q. D. 2005, MNRAS, 357, 1211
Schlafly, E. F., & Finkbeiner, D. P. 2011, ApJ, 737, 103
Shakura, N. I., & Sunyaev, R. A. 1973, A&A, 24, 337
Skrutskie, M. F., Cutri, R. M., Stiening, R., et al. 2006, AJ, 131, 1163
Stoop, M., van den Eijnden, J., Degenaar, N., et al. 2021, MNRAS, 507, 330
Strohmayer, T. E., & Smith, E. A. 2011, ATel, 3258, 1
Swank, J., & Markwardt, C. 2001, in ASP Conf. Ser. 251, New Century of X-ray Astronomy, ed. H. Inoue & H. Kunieda (San Francisco, CA: ASP), 94
Tetarenko, B. E., Sivakoff, G. R., Heinke, C. O., & Gladstone, J. C. 2016, ApJS, 222, 15
Timmes, F. X., Woosley, S. E., & Weaver, T. A. 1996, ApJ, 457, 834
Timmer, J., & König, M. 1995, A&A, 300, 707
Tody, D. 1986, Proc. SPIE, 627, 733
Tse, K., Galloway, D. K., & Heger, A. 2023, arXiv:2309.05236
Ubertini, P., Lebrun, F., Di Cocco, G., et al. 2003, A&A, 411, L131
van den Heuvel, E. P. J. 1992, in NATO Advanced Study Institute (ASI) Series C, Vol. 377, X-Ray Binaries and Recycled Pulsars, ed. E. P. J. van den Heuvel & S. A. Rappaport (Dordrecht: Springer), 233

van Paradijs, J. 1995, in X-ray Binaries, ed. W. H. G. Lewin, J. van Paradijs, & E. P. J. van den Heuvel (Cambridge: Cambridge Univ. Press), 536
Verner, D. A., Ferland, G. J., Korista, K. T., & Yakovlev, D. G. 1996, ApJ, 465, 487
Villa, G., Page, C. G., Turner, M. J. L., et al. 1976, MNRAS, 176, 609
Wagner, R. M., Foltz, C. B., Shahbaz, T., et al. 2001, ApJ, 556, 42
Walter, R., Bodaghee, A., Barlow, E. J., et al. 2004, ATel, 229, 1
Wang, A., Feng, H., An, T., et al. 2024a, ATel, 16817, 1
Wang, X.-L., Yan, Z., Xie, F.-G., Wang, J.-F., & Ma, R.-Y. 2024b, ApJ, 969, 152
Wei, J., Cordier, B., Antier, S., et al. 2016, arXiv:1610.06892
Weng, S.-S., & Zhang, S.-N. 2015, MNRAS, 447, 486
Wijnands, R., Degenaar, N., Armas Padilla, M., et al. 2015, MNRAS, 454, 1371
Wijnands, R., in't Zand, J. J. M., Rupen, M., et al. 2006, A&A, 449, 1117
Wijnands, R., & van der Klis, M. 1999, ApJ, 514, 939
Wilms, J., Allen, A., & McCray, R. 2000, ApJ, 542, 914
Winkler, C., Courvoisier, T. J. L., Di Cocco, G., et al. 2003, A&A, 411, L1
Wood, K. S., Ray, P. S., Bandyopadhyay, R. M., et al. 2000, ApJL, 544, L45
Yadav, J. S., Misra, R., Verdhan Chauhan, J., et al. 2016, ApJ, 833, 27
Yan, Z., & Yu, W. 2015, ApJ, 805, 87
Yang, Z.-X., Zhang, L., Zhang, S.-N., et al. 2024, ApJL, 970, L33
Yuan, F., & Narayan, R. 2014, ARA&A, 52, 529
Yuan, W., Dai, L., Feng, H., et al. 2025, SCPMA, 68, 239501
Yuan, W., Zhang, C., Chen, Y., & Ling, Z. 2022, Handbook of X-ray and Gamma-ray Astrophysics, Vol.86 (Singapore: Springer), 1
Yuan, X., Li, Z., Liu, X., et al. 2020, Proc. SPIE, 11445, 114457M
Zdziarski, A. A., Johnson, W. N., & Magdziarz, P. 1996, MNRAS, 283, 193
Zhang, B., Fan, Y. Z., Dyks, J., et al. 2006, ApJ, 642, 354
Zhang, S.-N., Li, T., Lu, F., et al. 2020, SCPMA, 63, 249502
Zhao, H.-S., Li, C.-K., Wang, J., et al. 2025, RDTM, 9, 215–222
Życki, P. T., Done, C., & Smith, D. A. 1999, MNRAS, 309, 561